2006

Investigation of Carbon Nanotube Growth Using a Nozzle CVD Method

James McFarland
Pomona College

Investigation of Carbon Nanotube Growth Using a Nozzle CVD Method

by

James McFarland

Advisor: Dr. David Tanenbaum

Senior Thesis

Submitted in partial fulfillment

of the requirements for the Degree of

Bachelors of Science in Physics

at Pomona College

April 2006

Table of Contents

1. Abstract

This work uses a modification of the chemical vapor deposition (CVD) technique to study the effects of source gas flow geometry (and the corresponding parameters) on carbon nanotube growth. Our approach is to flow the carbon-containing source gas through a nozzle, projecting the gas stream onto targeted regions of the substrate. This technique not only allows the potential for localized nanotube growth, but also offers an interesting opportunity to provide an experimental test of theoretical nanotube growth models.

Our results fail to show any significant nanotube growth for a wide range of parameters (most significantly source gas flow rate and nozzle aperture size), instead showing what we believe to be catalyst poisoning from excessive amorphous carbon deposition in almost all cases. A computational fluid dynamics (CFD) model is used to make predictions about methane pressures at the substrate surface for comparison with the data. Although no convincing conclusions can be drawn from our data, a simple model where the source gas partial pressure is the sole determinant of carbon decomposition does not seem to be supported. We suggest a number of experiments that could be pursued to investigate the interesting questions motivated and unanswered by the current work.

2. Introduction

Ever since their accidental discovery by S. Iijima, (Iijima, 1991) carbon nanotubes have provided a wealth of excitement for those looking to implement their interesting physical, electrical, mechanical, and chemical properties. There is a huge variety of potential applications for carbon nanotubes, the most prominent being uses in polymer composites, electrochemical devices, hydrogen storage containers, field emission displays, nano-electronic devices, probes, and sensors (Baughman et al., 2002). Currently, however, much of the research attempting to realize these applications is confronting similar difficulties controlling the location and properties of the nanotubes grown, and only recently have successful efforts been made to effectively address these issues. Furthermore, the general lack of control over the nanotube synthesis process speaks to the need for a detailed theoretical framework for nanotube formation, especially one that can account for the variety of techniques and conditions used to grow them.

This work attempts to address both of these issues by modifying the chemical vapor deposition (CVD) growth process with the potential to provide spatial control over the properties of the nanotubes grown. This is accomplished by injecting the source gas into the CVD furnace through a nozzle, confining the impinging source gas stream to a narrow region of the substrate surface. This method of nanotube localization has the potential advantage of simple and benign interfacing with almost any substrate, including those with topological complexity. Altering the source gas flow geometry also provides a means to make interesting and predictable changes to many of the parameters believed to be relevant for nanotube growth. The local effects of the flow geometry and source gas partial pressure (as well as their spatial derivatives) on nanotube growth have not been

well studied, and the characterization of these effects serves as the primary focus of this work.

Due to the poor theoretical understanding of the growth process it is impossible to fully anticipate the effects of such modifications to the CVD process, however possibilities include changes to the growth density as well as to the morphologies of the nanotubes grown. The former possibility is of particular interest, potentially addressing the previously mentioned problem of spatial control over the nanotubes grown. In analyzing our experimental results, we seek to make useful comparisons with the various theoretical models that have been proposed in order to better understand both the CVD growth process and the formation of nanotubes in general.

In order to make such comparisons and appreciate the purpose of this research, a foundational understanding of carbon nanotubes and how they are grown must first be established. To this end, the next section presents a general outline of the relevant theory including nanotube properties, growth methods, and theoretical growth models. Section 4 provides a brief overview of some of the relevant fluid dynamics equations that govern the gas flow. Section 5 moves on to review the related research that has been done at Pomona College leading up to this work. A detailed presentation of the procedure used in this experiment is offered in section 6 along with a description of the experimental apparatuses used, while section 7 presents our results. Section 8 discusses the computational fluid dynamics (CFD) simulation that was created to model the experiment, as well as the results obtained from the modeling. Section 9 contains data analysis, including a discussion of the modeling results and how the data compare with

existing theoretical models. A discussion of potential directions for future research based on this work is given in section 10, and finally conclusions are discussed in section 11.

3. Theory

3.1. Nanotube Basics

A carbon nanotube is essentially a single sheet of graphite (known as *graphene)* that has been rolled into a cylinder (Figure 1).

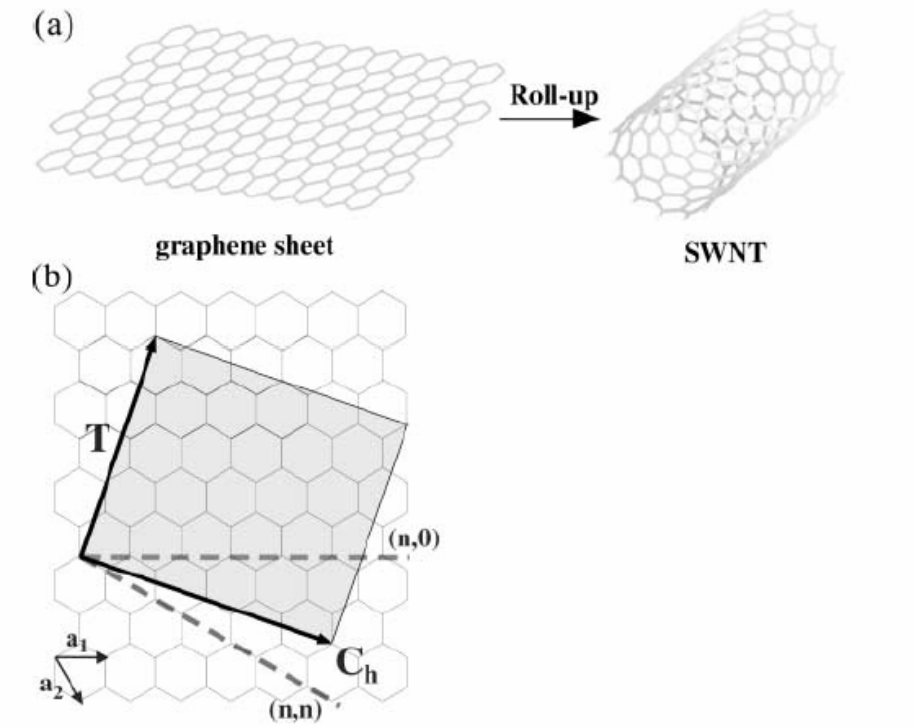

Figure 1 (Lieber et al., 2001)
(a) shows a graphene lattice being rolled into a single-walled nanotube (b) depicts how the orientation of the roll-vector Ch effects the geometry of the nanotube obtained.

Theoretical nanotubes are thought of as being closed on one or both ends by a hemispherical fullerene cap, however no intact caps have been observed (Hirsch, 2002). Instead, the ends of the nanotubes are often found to be closed by metal catalyst particles (see Section 3.3.2) or bound directly to the surface.

As might be expected, geometrically unique carbon lattices can be obtained by rolling the graphene sheet in different directions to create nanotubes with different helicities (Figure 1b). The 'roll vector,' which is characterized by two parameters (*n, m*), classifies the nanotube as one of three main types, armchair ($n = m$), zigzag ($n = 0$ *or,* $m = 0$), and chiral (*other*); the primary significance of the roll vector being that it determines the band structure of the nanotube (roll vectors with $(n-m)/3 =$ an integer correspond to metallic tubes while other roll vectors produce semiconducting tubes) (Figure 2).

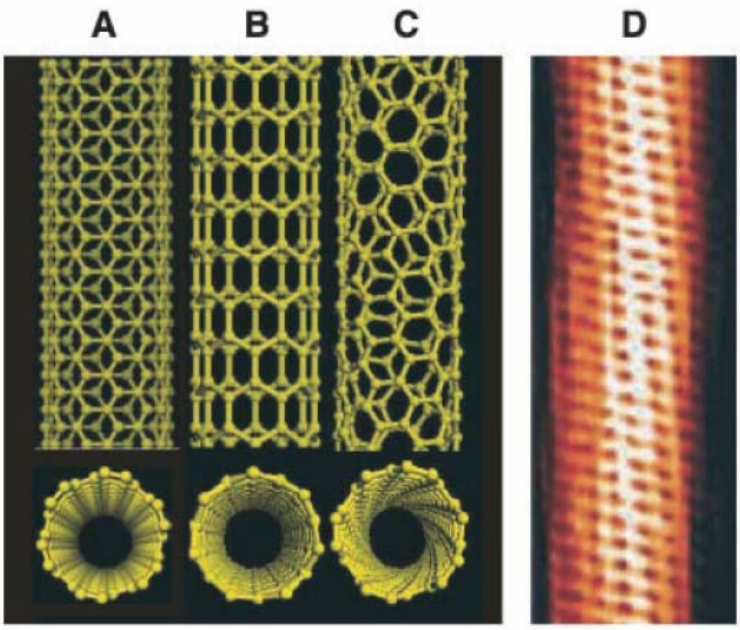

Figure 2 (Baughman et al., 2002)
*Different types of nanotubes: (**A**) armchair (**B**) zigzag (**C**) chiral (**D**) TEM image of a nanotube.*

Nanotubes can also be either single-walled (SWNT) or can exist in more complex morphologies including: concentrically arrayed multi-walled nanotubes (MWNT), bundles or sheets of aligned SWNTs, and even mats and ropes of SWNTs and MWNTs (Baughman et al., 2002). In general nanotubes of the single-walled variety, with

diameters on the order of 1 nm, have more desirable chemical and electronic properties, and can be described by simpler one-dimensional models. Their simplicity and functionality make methods for highly selective growth of single-walled nanotubes (SWNTs) often desirable, however, bundles of aligned SWNTs are thought to share many of the one-dimensional quantum properties of unbundled SWNTs, and MWNTs have many potential applications as well (Baughman et al., 2002).

3.2. Nanotube Properties

A brief overview of some of the more unique properties of carbon nanotubes is presented to further motivate the desire to achieve controlled growth. Firstly, carbon nanotubes are extremely mechanically strong, having density-normalized Young's moduli and tensile strengths of 19 times and 56 times that of steel wire respectively. Additionally, due to the essentially one-dimensional nature of the nanotubes, SWNTs as well as MWNTs exhibit quantized conductances and conduct current ballistically (without scattering) when the effects of lattice defects and surface contacts are ignored. The low heat dissipation and extremely large current densities implied by these characteristics have been demonstrated experimentally (de Heer et al., 1998). Phonon transport also occurs quite easily along the length of a nanotube, giving MWNTs thermal conductivities greater than that of diamond (Baughman et al., 2002). Because of their extremely small diameter, application of an electric potential to a nanotube will produce large local electric fields making them ideally suited for use in field-emission devices.

In general, perfect SWNTs are chemically inert, however, due to the angle strain of the sp^2-hybridized carbon atoms, as well as the misalignment of the carbon π-orbitals, nanotubes are more reactive than their graphene counterparts (Haddon et al., 2002).

Nanotube reactivity often comes in the form of structural defects in the sidewalls that are observed to occur in normal growth processes, and can be introduced under oxidative conditions. These defects can then be used to attach various functional groups to the nanotubes to achieve chemical functionalization (Hirsch, 2002).

Perhaps the most significant excitement surrounding carbon nanotubes, however, has centered around their implementation in nanoscale electrical devices. Again, because they can exist in either a metallic or semiconducting form, nanotubes could potentially be used as both wires and transistors in nanoscale electronic devices. Significant progress has been made towards this end with demonstrations of both p and n-type nanotube field-effect transistors (FETs) (Figure 3), FET arrays, and even integrated circuits of nanotube transistors (Avouris, 2002) and nonvolatile memory (Lieber et al., 2000).

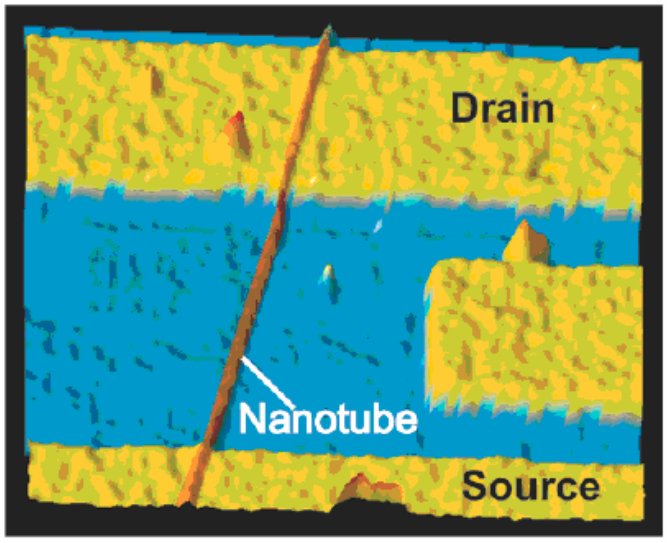

Figure 3 (Avouris, 2002)
AFM image of a carbon nanotube field-effect transistor

One trend that is easily apparent among these potential applications is the need for at least some degree of control over the location of the nanotubes, as well as their properties (SWNTs vs MWNTs, semiconducting vs. metallic, length, diameter, density of

tubes, etc.). Before discussing possible approaches to achieving such control, I discuss common nanotube growth techniques.

3.3. Nanotube Growth

Carbon nanotubes are typically grown using either laser ablation, carbon arc discharge, or chemical vapor deposition (CVD) methods. All of these synthesis techniques share several important similarities; namely, they all involve a source of carbon, a source of heat, some form of metal catalyst, and usually take place in an inert gas environment. In the laser ablation method, pulsed lasers impinge upon a composite of graphite and metal catalyst, vaporizing the carbon. Similarly, in the carbon arc discharge method catalyst-containing carbon electrodes are vaporized by an electric discharge in an inert chamber (Awasthi et al., 2005). Chemical vapor deposition is the most popular growth method, and it differs from the other methods in that the carbon is provided by flowing some carbon source gas through a furnace containing catalyst deposited on a (usually) silicon substrate. In each case, it is believed that the gas-phase carbon then condenses onto the surface of the catalyst to form the nanotubes.

3.3.1. Chemical Vapor Deposition

The focus of this review will be on the chemical vapor deposition technique since it is used in this work. As previously described, the CVD process consists of a carbon-containing source gas introduced to a substrate (containing deposited catalyst) situated inside of a furnace under an inert gas atmosphere (Figure 4).

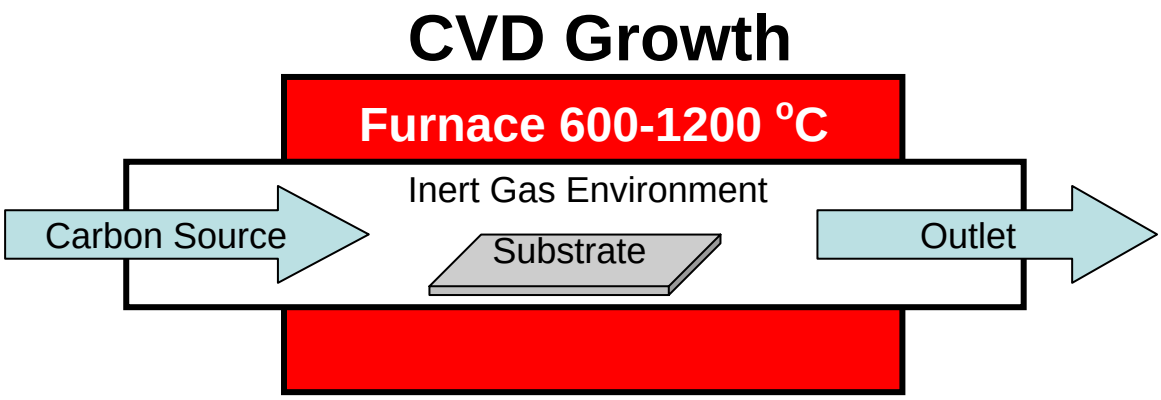

Figure 4
Schematic diagram of the CVD growth apparatus with a carbon source gas, hydrogen, and an inert gas being flowed through a furnace containing a growth substrate.

Successful nanotube growth has been demonstrated over a fairly large volume of parameter space including usage of various source gases and source gas flow rates, catalyst metals, deposition techniques and concentrations, furnace temperatures, and even with the inclusion of various additive gases. No single set of CVD growth parameters has become widely accepted, and a choice of parameters often involves tradeoffs between the quantity and quality of nanotubes grown.

A number of different carbon source gases can be used including CO, CH_4, C_2H_2, C_6H_6, and C_8H_{10} (Vander Sande et al., 2005). It is even possible to use an inert gas bubbled through ethanol as a carbon source gas (Maruyama et al., 2004). In addition to the range of possible source gases, a wide range of flow rates can be used, with the optimal rate depending on the choice of source gas. Similarly, optimal growth temperatures vary significantly depending on the choice of source gas, catalyst, etc., ranging from 600 °C (Salernitano et al., 2004) to 1200 °C (Smalley et al., 1999). Although not typically considered a critical parameter in CVD growth (most growths are conducted under atmospheric pressure), the growth can also be conducted under various

pressures, and nanotube growth has been demonstrated at pressures ranging from 20 mbar (Salernitano et al., 2004) to 10 atm (Smalley et al., 1999).

Several additive gases including sulfur, ammonia, nitrogen and hydrogen can be injected into the furnace during growth to induce a number of interesting effects on nanotube growth (Vander Sande et al., 2005). By far the most commonly used of these is hydrogen which is thought to have a number of beneficial effects on the growth process. Hydrogen is often thought to satisfy dangling bonds at the edge of graphite planes (Vander Sande et al., 2005), as well as etch away non-nanotube carbon phases (Schlapback et al., 1998). Hydrogen also reduces metal oxides and increases the mobility of the metal catalyst, allowing it to spread and assume more deformed morphologies thought to assist in the growth process (Schlapback et al., 1998).

Additive gases can also be used to shape specific aspects of the nanotubes grown. For instance, exposure to oxygen has been shown to dramatically alter the electronic properties of nanotubes, potentially acting as a p-type dopant for semiconducting nanotubes, and has even been shown to convert semiconducting tubes into metallic ones (Zettl et al., 2000). Additionally, the presence of nitrogen (in the form of ammonia) has been found to increase the alignment of the nanotubes grown when using ethylene as a source gas (Vander Sande et al., 2005). Perhaps the most critical parameter of all in the CVD growth process, however, is the choice of catalyst metal and the method by which it is deposited on the substrate.

3.3.2. Catalyst

Although transition metals such as iron, nickel, cobalt, and their alloys are by far the most commonly used catalysts, other metals such as palladium, molybdenum, and

magnesium alloys have been used as well (Dupuis, 2005). While many metals will work as catalysts, the bulk metals themselves are not effective (for instance, bulk iron will not decompose methane), and thus various methods must be used to disperse the catalyst metals in the form of nanoparticles (Dupuis, 2005). These nanoparticles are typically in the 10 – 100 nm range, with smaller particles thought to poison the support surface and larger ones being unable to catalyze NT growth (Dupuis, 2005).

Many techniques exist for delivering catalyst nanoparticles, the simplest of which is to deposit them directly onto the substrate in solution followed by drying of the solvent. When depositing catalyst in solution it is common to use porous support particles such as alumina or silica. Although the precise nature of the catalyst-support particle interaction is unclear, it is believed that the porous support particles increase the efficiency of nanotube growth by providing active catalyst sites. Substantial differences in growth efficiency and morphologies are observed for different catalyst/support combinations, and at least part of the effect of the support particles is believed to be due to their specific structure. For example, alumina (which is the support used in this work) has been shown to give excellent yields of individual SWNT's when coupled with iron catalyst particles. One proposed explanation for the observed lack of nanotube clumping is that the crystal edges of the anisotropic Al_2O_3 nanocrystals give more dispersed and varying active catalyst sites when compared to silica supports (which tend to yield bundles of SWNT's) (Kong et al., 1998). Alternative methods of catalyst deposition include the use of sol gels, chemical reactions on the substrate, micelles, CVD deposition of metalorganic precursors, thermal decomposition of carbonyl complexes, and thin film growth (either by evaporating or sputtering) (Dupuis, 2005).

In addition to depositing catalyst in solution, a number of our experiments employed the evaporation of thin catalyst films. These transition metal thin films are thought to be initially smooth, assuming more rounded morphologies associated with nanoparticles only upon annealing. It has been shown that the size of the nanoparticles formed is directly related to the thickness of the deposited film, and this is used to control with relatively high precision the size distribution of deposited particles (Dupuis, 2005). The presence of hydrogen during the annealing of the film is thought to increase the wetting of the catalyst, assisting in the dispersion of the deposited film on the substrate (Dupuis, 2005); and it has been suggested that such liquid-phase catalyst particles are necessary for the growth of SWNTs (Vander Sande et al., 2005). Having discussed the processes used to grow NTs, and some of the considerations requisite in these methods, we now move on to consider techniques used to control the growth of NTs.

3.3.3. Growth Control

Control over the characteristics of NTs can often be obtained simply by varying the relevant parameters (type of catalyst, method of catalyst deposition, carbon source, etc). For example, by changing the preparation of the substrate, Pan et al. (1998), were able to grow extremely long (several mms) MWNTs. Similarly, the use of iron as a catalyst has been shown to yield the highest density of carbon structures (but generally of lower quality), while the use of alloys of cobalt, iron, or nickel as catalyst has been shown to increase the yield of SWNTs relative to MWNTs (Dupuis, 2005). Even the separation of semiconducting NTs from metallic NTs has been achieved using AC dielectrophoresis (Kappes et al., 2003).

Control over nanotube orientation has been demonstrated in the creation of large, well-aligned MWNT arrays that have been constructed using several different techniques including: embedding the catalyst particles in a porous silica substrate (Provencio et al., 1998), applying an AC electric field to nanotubes in solution (Hilding et al., 2005), as well as using a microwave plasma enhanced CVD technique (Choi et al., 2000). Additionally, significant work has been done demonstrating the growth of ultradense 'forests' of vertically oriented nanotubes using a variety of techniques, perhaps most interesting being a water-assisted CVD method (Hata et al., 2004). Although vertically oriented nanotubes are extremely interesting, we focus on techniques for growing lower density planar nanotubes as these are the types of nanotubes we are investigating in this work.

An alternative technique for controlling nanotube alignment is achieved by the use of a rapid-heating CVD method (Huang et al., 2003). In this procedure, substrates containing catalyst nanoparticles are quickly introduced from room temperature into a 900 ^{o}C CVD furnace, heat shocking the catalyst particles and causing them to jump off the substrate into the air. A 'flying catalyst' model where the nanotube grows in the wake of the airborne catalyst (a 'base growth' model, Section 3.4.3) is then suggested to explain the observed nanotube orientations, which can be controlled by manipulating the gas flow in the furnace. This technique can even be used to create 2D networks of aligned nanotubes.

Perhaps the most important step towards the functionalization of carbon nanotubes is attaining precise and reproducible control over the spatial location of the nanotubes. Specific regions of nanotube growth can easily be achieved by

lithographically defining regions of deposited catalyst ('catalyst pads'). In this technique, the nanotubes grow not only on the pads, but also extending outward from the pads, thus allowing the possibility of having individual nanotubes span predetermined gaps between catalyst pads. Once such a nanotube is obtained, measurements of single NT properties are possible; however, such a 'guess and check' method is clearly insufficient for attaining localization in scalable applications. Another method of controlled nanotube placement is to deposit a suspension of NTs onto a substrate with lithographically defined regions of chemically-functionalized SiO_2 that actively absorb the NTs (Tsui et al., 2002). Alternatively, single NTs can be picked up and deposited in precise locations using an atomic force microscope (AFM) tip (Superfine et al., 2002); however, this approach is extremely slow and cumbersome. Perhaps the most precise demonstration of the controlled deposition of individual NTs involves mechanically transferring carefully grown, suspended NTs by physically contacting the suspended NTs with an adhesive region at the target location (Hone et al., 2005).

Alternatively, localized growth can be attained by controlling the local partial pressure of the source gas or the local temperature with sufficient precision to exclusively allow tube growth at predetermined locations. The use of microhotplate arrays as localized heat sources for CVD nanotube growth has already been demonstrated, and provides a convenient approach to performing parallel studies of the effects of temperature on the nanotube growth process (Turner et al., 2004). Both the size of the microhotplates (typically around 100 μm) as well as their requisite presence on the substrate serve to limit the precision and functionality of this approach.

As far as this author is aware, to date there has been no successful demonstration of localized growth using the spatial control of source gas density. If the source gas could be introduced at site specific locations on a substrate, potentially through the use of a gas-injection nozzle, it could be possible to localize nanotube growth by limiting sites with the carbon availability requisite to grow nanotubes. This type of gas-localization nozzle could potentially be automated and used to 'spray' a substrate with a predefined geometry of nanotubes. Such a method would have the advantage of interfacing with a wide range of substrates, including ones with significant topological complexity. Any approach to achieving control of this kind, however, requires a careful investigation of the available theoretical models for nanotube growth.

3.4. Growth Models

There have been many models put forth to describe nanotube growth, each usually targeted to a specific growth process under a specific range of conditions. Any comprehensive model would need to account for the different growth methods, and even a model targeted towards CVD growth alone would need to explain the huge range of parameters that have been successfully used. No such model has yet been proposed, however, a number of models have had significant success predicting experimental results under limited sets of growth conditions, with nearly all of these sharing three distinct steps: catalytic decomposition of the source gas to form solid carbon, diffusive transport of carbon through the metal, and precipitation of a nanotube on the surface of the catalyst (Figure 5) (Vander Sande et al., 2005).

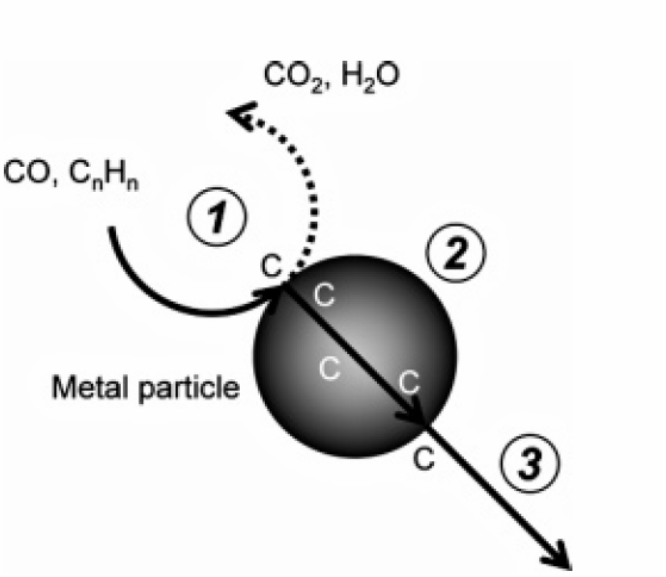

Figure 5 (Vander Sande et al., 2005)
*The basic nanotube growth mechanism consists of three steps (**1**) carbon decomposition (**2**) diffusive transport and (**3**) precipitation.*

3.4.1. Decomposition

Three possible reactive processes can lead to the catalytic decomposition of elemental carbon at the surface of the metal including cracking, reduction, and disproportionation, and the dominant reaction depends largely on the source gas used (Figure 6). Because we use methane as a source gas, cracking is the relevant process for this work.

$$C_xH_y \xrightarrow{\text{metal}} xC_{\text{solid}} + \frac{y}{2}H_2 \quad \text{cracking}$$

$$CO + H_2 \xrightarrow{\text{metal}} C_{\text{solid}} + H_2O \quad \text{reduction}$$

$$2CO \xrightarrow{\text{metal}} C_{\text{solid}} + CO_2 \quad \text{disproportionation}$$

Figure 6 (Vander Sande et al., 2005)
Reaction mechanisms leading to catalytic decomposition of carbon from a gas-phase source.

It has been shown that the rate of carbon deposition depends on the concentration of source gas, however, other factors such as the presence of additive gases (CO_2, H_2O, and H_2) can also affect the deposition rate (Vander Sande et al., 2005).

The most effective metal catalysts (iron, nickel, and cobalt) allow rapid internal (bulk) and surface diffusion (Derbyshire et al., 1999). While theoretical predictions indicate that for length scales of the order of the diameter of a typical catalyst particle (10 nm), bulk diffusion should dominate surface diffusion, it has been suggested that if deposition rates overwhelm internal diffusion the catalyst particle can become coated with carbon, deactivating the growth process (Vander Sande et al., 2005), and these predictions agree with experimental observations (Li et al., 2006).

3.4.2. Diffusion

Some authors attribute the cause of the subsequent diffusive transport to an internal temperature gradient that develops as a result of exothermic decomposition of carbon on one side of the catalyst and endothermic carbon precipitation at the other end (Dupuis, 2005). Others attribute the diffusion to a concentration gradient that develops across the catalyst particle, however the origin of such a concentration gradient is somewhat disputed (Vander Sande et al., 2005). An 'interacting particle' model was recently proposed suggesting that two catalyst particles must coalesce to form a dimer, blocking carbon deposition at the point of coalescence and establishing the necessary concentration gradient across the particles, with a net diffusive flux developing toward the coalescence point. This model led to predictions of nanotubes growing between the two catalyst particles producing 'dumbbell-shaped' morphologies that have been observed experimentally under certain growth conditions (Vander Sande et al., 2005).

This same model predicted that the growth stage should remain stable as long as conditions such as temperature and source gas concentration remain relatively constant as the tube grows, leading to production of longer nanotubes in steady conditions.

3.4.3. Precipitation

The final step in nanotube growth, precipitation of carbon at the catalyst surface, is often thought to occur by the formation of a hemispherical cap of carbon which then lifts off of the surface with nanotube growth in the wake of the cap (a 'base growth' mechanism). The formation of the hemispherical cap is highly favorable because it satisfies dangling bonds that would inevitably result at one end of a nanotube (Dai et al., 1996). Cap formation, followed by nanotube growth, has been shown to occur spontaneously in molecular dynamics simulations of the CVD process. This model also showed that caps with roughly the same diameter as the catalyst particles they form on are much more stable and more likely to lead to NT growth than caps of other sizes, a prediction which agrees with many experimental observations of nanotube size distributions being tightly correlated with catalyst particle size distributions (Balbuena et al., 2005).

Alternatively, nanotube growth has been suggested to occur with one end of the nanotube bound to the substrate and the catalyst particle growing outwards from the substrate (a 'tip growth' mechanism). In such cases, it has been hypothesized that the internal lattice structure of the metal particle could constrain the precipitating carbon into a more stable geometry, thus avoiding much of the bond strain associated with the formation of a cylindrical graphene lattice. Although this energy barrier to nanotube

formation is quite significant, once formed, the cylindrical lattice minimizes dangling bonds, and is approximately as stable as a graphene sheet (Vander Sande et al., 2005).

4. Fluid Mechanics

The general equation that governs the flow of an incompressible fluid is known as the Navier-Stokes equation and its local (differential) form is given by:

$$\rho \frac{\partial \vec{v}}{\partial t} + \rho(\vec{v} \cdot \nabla)\vec{v} = \rho\vec{f} - \nabla p + \eta \nabla^2 \vec{v}\,, \tag{1}$$

where $\vec{v}(\vec{r},t)$ is the vector velocity field, ρ is the fluid density, $p(\vec{r},t)$ is the scalar pressure field, $\vec{f}$ is the externally applied volume force, and η is the viscosity of the fluid. We can qualitatively understand the meaning of each of these terms by considering their meaning for a single fluid particle. The first term on the left is an acceleration attributed to the explicit time dependence of the velocity field. Similarly, the second term on the left is an acceleration that is caused by the convective flow of the particle through the velocity field (e.g. even a time-independent velocity field changes as the particle moves through its trajectory). The first term on the right-hand side of equation (1) gives the acceleration due to any external volume forces applied to the fluid. The ∇p term is easily understood as the force created by a gradient in the pressure, and the final term (which is more complicated in the case of a compressible fluid) represents the viscous forces on the fluid element (Guyon et al., 2001).

Another important concept in fluid dynamics is that of the Reynolds Number, which is given by:

$$\mathrm{Re} = \frac{\rho U^2}{\eta U / L} = \frac{\rho U L}{\eta}\,, \tag{2}$$

where U is a characteristic velocity, and L is a characteristic length of the flow. The first expression in equation (2) makes the Reynolds number easily comprehensible as the ratio of convective (due to kinetic energy) to diffusive (via viscous forces) momentum transfer processes. Different flow regimes can qualitatively be distinguished on the basis of this dimensionless number, with turbulence occurring for high Reynolds flows. In general flows with $Re >> 100$ are probably turbulent while flows with $Re << 100$ are likely laminar, however this is only a rough distinction.

The finite volume methods used by Fluent (the computational fluid dynamics software package used to create our simulation) employ spatial discretization of the geometry in order to solve the relevant equations for the conservation of mass, momentum, and energy in each discrete volume element. Starting with an initial guess for each of the parameters, Fluent then iterates the solution of the conservation equations (independently of one another in the case of the segregated solver) as shown in Figure 7, checking for convergence of the residuals after each iteration.

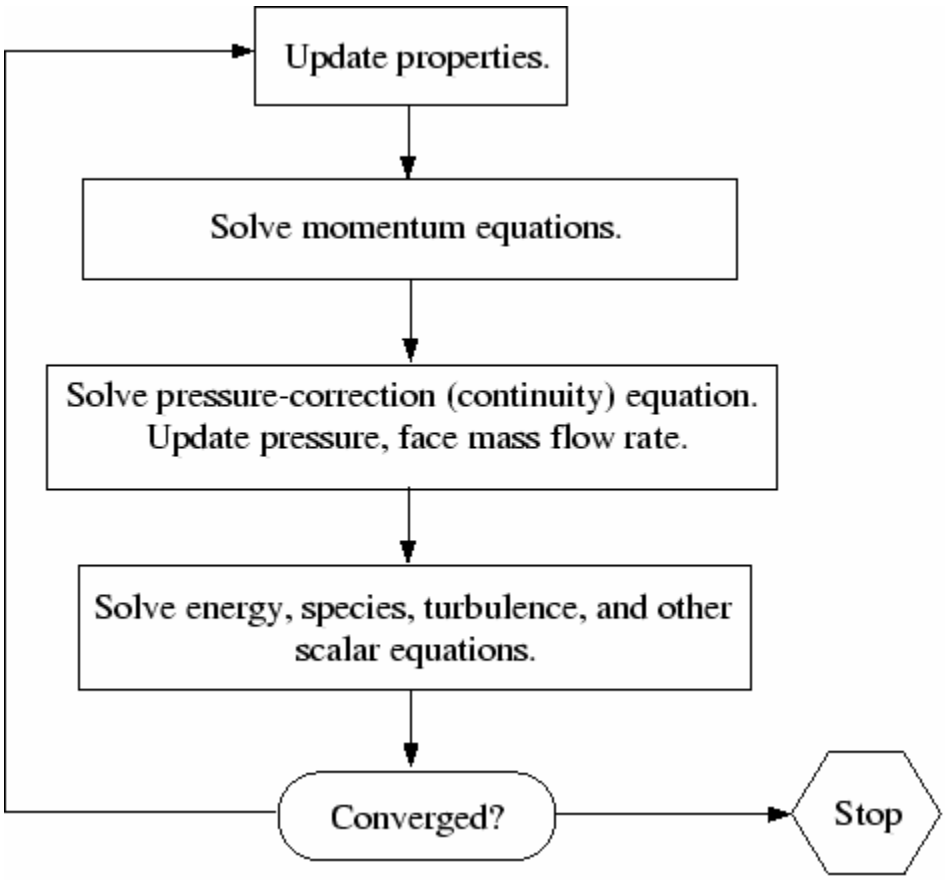

Figure 7 (Fluent, Inc.)
Flow diagram showing the steps used by Fluent to iteratively solve the governing fluid equations in the segregated solver.

The iterations stop once a predefined upper limit on these residuals has been reached, and a solution with the desired accuracy has been obtained (Fluent, Inc.).

The conservation equations Fluent employs are integral equations that can be considered separately in each local volume element, however I present the corresponding equations in differential form for simplicity. The continuity equation (conservation of mass) is given by:

$$\frac{\partial \rho}{\partial t} + \nabla(\rho \vec{v}) = S\,, \tag{3}$$

where S represents a source term for the mass. In the case where we are not considering chemical reactions or phase changes we can set $S = 0$, and equation 3 reduces to:

$$\frac{\partial \rho}{\partial t} + \rho \nabla \cdot \vec{v} = 0 \,, \tag{4}$$

which in the case of 2-dimensional axisymmetric geometries becomes:

$$\frac{\partial \rho}{\partial t} + \frac{\partial}{\partial z}(\rho v_z) + \frac{\partial}{\partial r}(\rho v_r) + \frac{\rho v_r}{r} = 0 \,. \tag{5}$$

Similarly, the equation governing the conservation of momentum is given by:

$$\frac{\partial}{\partial t}(\rho \vec{v}) = -\nabla \cdot (\rho \vec{v}\vec{v}) - \nabla p + \nabla \cdot \left(\bar{\bar{\tau}}\right) + \rho \vec{g} + \vec{F} \,, \tag{6}$$

where $\bar{\bar{\tau}}$ represents the stress tensor and $\vec{F}$ is any external body force (Fluent, Inc.). This equation can be understood more intuitively by defining a quantity called the momentum flux tensor given by:

$$\Pi_{ij} = \rho v_i v_j + p\delta_{ij} - \tau_{ij} \,. \tag{7}$$

This quantity gives the transport of the *ith* component of the momentum by particles moving in the *jth* direction due to convection, pressure forces, and viscous friction forces respectively (Guyon et al., 2001). In the case of 2-dimensional axisymmetric geometries, equation 6 gives the axial momentum conservation equation (Fluent, Inc.):

$$\begin{aligned} &\frac{\partial}{\partial t}(\rho v_z) + \frac{1}{r}\frac{\partial}{\partial z}\left(r\rho {v_z}^2\right) + \frac{1}{r}\frac{\partial}{\partial r}(r\rho v_r v_z) = -\frac{\partial \rho}{\partial z} \\ &+ \frac{1}{r}\frac{\partial}{\partial z}\left[r\left(\mu 2\frac{\partial v_z}{\partial z} - \frac{2}{3}(\nabla \cdot \vec{v})\right)\right] + \frac{1}{r}\frac{\partial}{\partial r}\left[r\mu\left(\frac{\partial v_z}{\partial r} + \frac{\partial v_r}{\partial z}\right)\right] + F_z \end{aligned} \,, \tag{8}$$

and the radial momentum conservation equation:

$$\frac{\partial}{\partial t}(\rho v_r)+\frac{1}{r}\frac{\partial}{\partial z}(r\rho v_z v_r)+\frac{1}{r}\frac{\partial}{\partial r}(r\rho v_r{}^2)=-\frac{\partial \rho}{\partial r}+\frac{1}{r}\frac{\partial}{\partial z}\left[r\mu\left(\frac{\partial v_r}{\partial z}+\frac{\partial v_z}{\partial r}\right)\right]+$$
$$\frac{1}{r}\frac{\partial}{\partial r}\left[r\mu\left(2\frac{\partial v_r}{\partial r}-\frac{2}{3}(\nabla\cdot\vec{v})\right)\right]-2\mu\frac{v_r}{r^2}+\frac{2}{3}\frac{\mu}{r}(\nabla\cdot\vec{v})+\rho\frac{v_z{}^2}{r}+F_r \quad (9)$$

If heat transfer is included, a third conservation equation for energy must also be included. The conservation of energy equation is given by:

$$\frac{\partial}{\partial t}\left(\frac{\rho v^2}{2}\right)+\nabla\cdot\left[\vec{v}\left(\frac{\rho v^2}{2}+p\right)\right]=\nabla\cdot\left(\kappa_{eff}\nabla T+\left(\bar{\bar{\tau}}_{eff}\cdot\vec{v}\right)\right)+S_h, \quad (10)$$

where the two terms on the right hand side give the energy transfer due to conduction (where $\kappa_{eff}=\kappa+\kappa_t$, κ_t being the turbulent thermal conductivity) and viscous dissipation respectively (Fluent, Inc.). S_h represents a source term, which in our case accounts for radiative energy transfer. As will be discussed more thoroughly in section 8, Fluent employs these three conservation equations to provide numerical solutions for many of the parameters of interest in our experiment.

5. Previous Research

A significant amount of research has already been conducted to establish procedures for the growth and characterization of nanotubes at Pomona College. A foot long furnace with a three foot long, one-inch quartz tube running through it is used in conjunction with individually controlled flows of methane, hydrogen, and argon to achieve chemical vapor deposition. Previous experiments have used an iron catalyst deposited in solution (either with or without alumina support particles), both isotropically and with catalyst pads defined using maskless projection photolithography (Ferguson, 2003). Our samples have traditionally been analyzed using a Dimension 3100 Atomic Force Microscope (AFM), however we recently acquired a Leo 982 Field-Emission

Scanning Electron Microscope (FESEM) which we now use primarily for sample analysis.

5.1. Furnace Temperature

In order to achieve a better understanding of the thermal conditions inside the furnace, and to provide data for the Fluent model (Section 8) we took temperature measurements along the furnace tube axis. To measure this temperature variation a thermal couple was used to sample the temperature at roughly 0.5 cm increments over a range of 16 cm around the center of the furnace. Under 'typical' conditions, with the furnace set at 980 ^{o}C and argon flowing at 1 standard liter per minute (SLM), the actual temperature 6.5 cm upstream of the furnace center was found to be 948 ^{o}C, whereas the corresponding temperature 6.5 cm downstream was found to be 974 ^{o}C. These values are to be compared with a maximum value of 986 ^{o}C, which is constant over the range of 1 – 3.5 cm downstream of the furnace center (Figure 8).

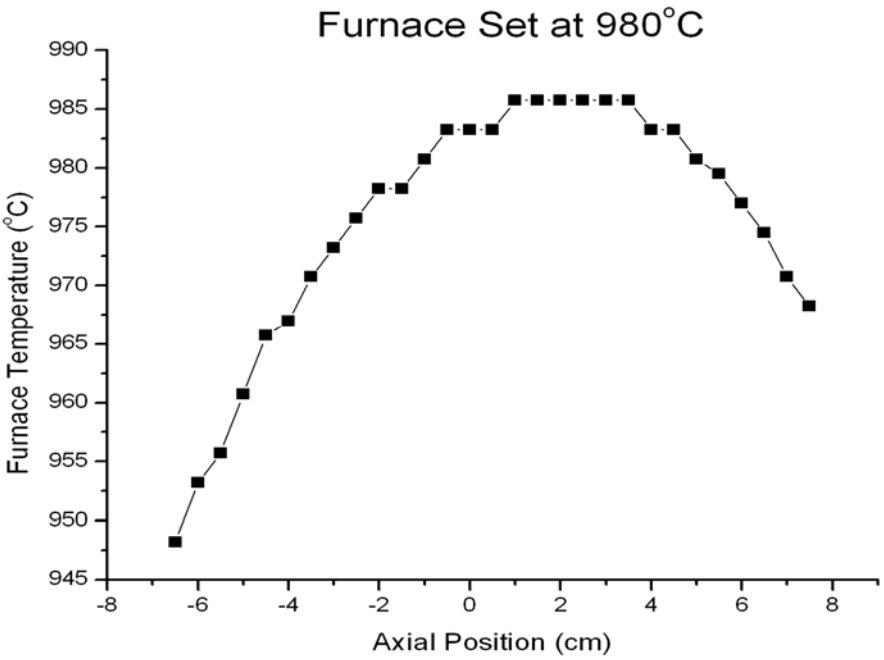

Figure 8

Plot showing the Furnace temperature as a function of axial displacement from the center of the furnace.

From figure 8, we see that while there is significant temperature fluctuation along the furnace axis, the temperature in the 3 cm area surrounding the center is constant to within 8 ^{o}C, and there is a region of excellent special invariance extending from the center of the furnace 4.5 cm downstream. These results suggest that if substrates are confined to the central region of the furnace (or perhaps slightly downstream of the furnace center), the temperature should be relatively invariant.

5.2. Catalyst Experiments

We have traditionally deposited catalyst directly in solution, using methanol based solutions of alumina supported iron catalyst. This catalyst has been shown to give high yields of nanotubes both in previous work at Pomona (Ferguson, 2003), and in work by other authors (Kong et al., 1998, Hafner et al., 1998). Unfortunately, we have also

found that this catalyst tends to yield shorter nanotubes, and can produce unwanted carbonaceous materials. These carbonaceous deposits, along with the alumina catalyst particles themselves (which have a broad size distribution typically on the order of several microns) reduce the functionality of these samples for many relevant applications. Additionally, the majority of the nanotubes tend to be found in dense clusters around the alumina particles making them difficult to access for experimentation and functionalization (Figure 9).

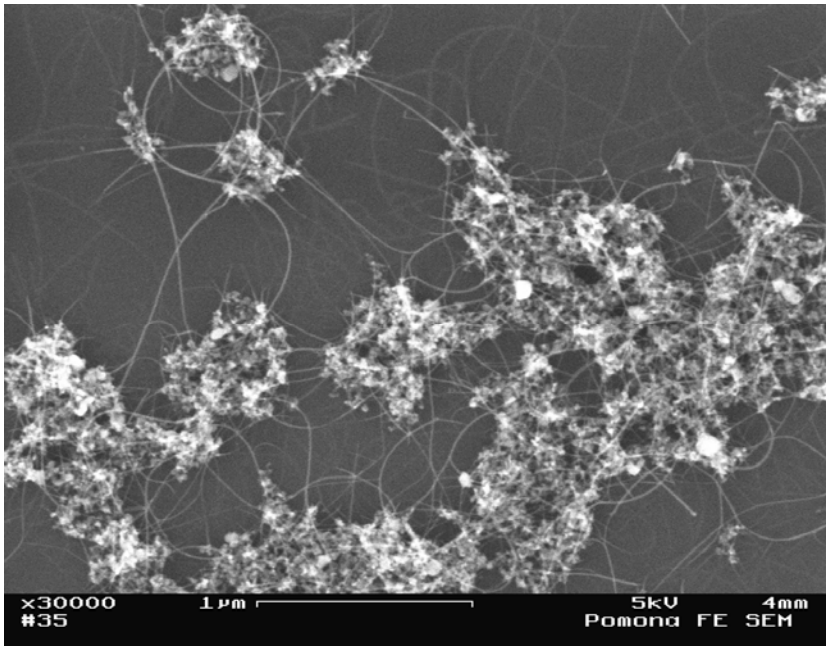

Figure 9
SEM image of carbon nanotubes growing from catalyst particles embedded in clusters of alumina support particles.

We found that most of these issues can be avoided by using an isopropyl alcohol (IPA) based iron catalyst solution (without alumina support) grown with ethylene (rather than methane) as a source gas (McFarland and Scire, 2002). This catalyst tends to produce much cleaner samples (avoiding alumina debris and much of the carbonaceous material deposited with the previous catalyst solution) while still giving good yields of

SWNTs. Other approaches, including the use of solutions of iron nanoparticles, have been demonstrated by Pomona students (Frank, 2005), however, the robustness, high nanotube yields, and ease of imaging associated with the alumina supported iron catalyst make it a desirable choice when attempting to demonstrate nanotube growth with a novel technique (as in the present work).

Yet another approach to catalyst deposition is the evaporation of thin films. This technique has recently been demonstrated at Pomona using a homemade evaporation chamber (Penilla, 2006). Although extremely attractive for the simple creation of catalyst pads (using a shadow mask during the evaporation process), we have found both advantages and disadvantages of evaporated catalyst compared to solution based catalysts. Firstly, while the thin film growths tend not to produce as high a nanotube yield, the growths do exhibit high SWNT selectivity, the nanotubes produced are usually much longer (as long as several hundred microns), and the substrates are substantially cleaner outside of the catalyst 'pads' (Figure 11).

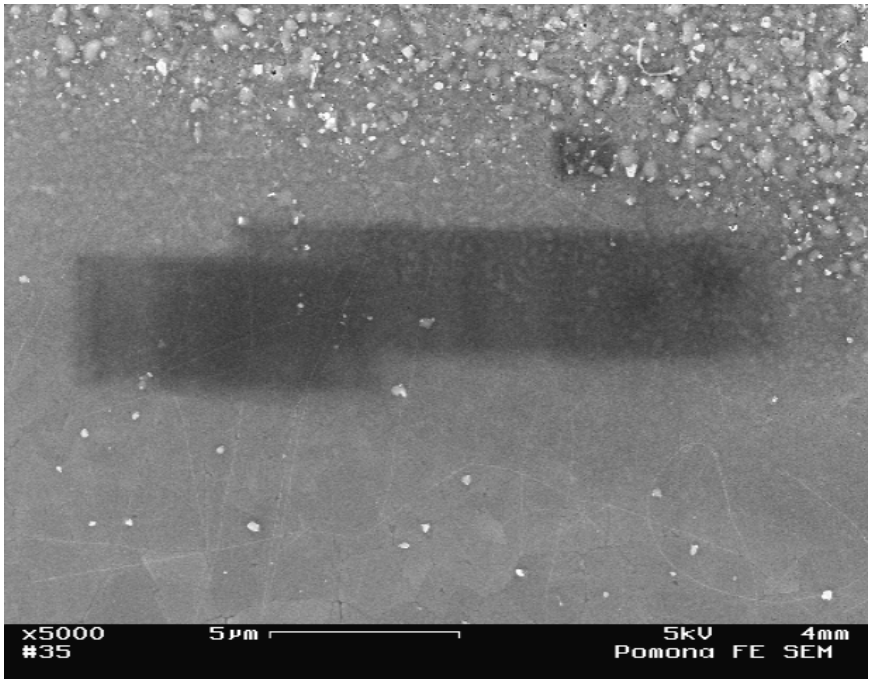

Figure 11 (Penilla, 2006)
SEM image of nanotubes growing from the evaporated catalyst pad near the top of the image (the dark regions are an residue from previous imaging).

One drawback we have found with this technique is that it exhibits a high sensitivity to the thickness of the catalyst film. The range of film thicknesses for which the catalyst seems to be effective is in the submonolayer regime, and likely spans only several angstroms. Additionally, hydrogen gas seems to play a critical role in dispersing the catalyst during the growth process (Section 3.3.2) and the associated flow rate is another parameter that must be carefully controlled. Considering the advantages and problems associated with each technique, both the evaporated and solution-based catalysts are tested in this study.

5.3. Optical Fiber Experiments

Some of our previous experiments have attempted to localize methane flow at specific points on the substrate by flowing the source gas through a hallow-core optical

fiber. To do this we used a 13.5 inch piece of hallow-core optical fiber with an inner diameter of 150 microns and an outer diameter 360 microns. The polyimide coating surrounding the fiber was removed by heating it in a furnace at 650 ^{o}C for 30 minutes. The segment of optical fiber was then passed through a small hole in a rubber stopper, and was sealed to that hole using silicone rubber. Because the bare optical fiber (without the polyimide coating) was extremely brittle, it was necessary to support the length of fiber extending into the furnace inside of a larger quartz tube (Figure 12).

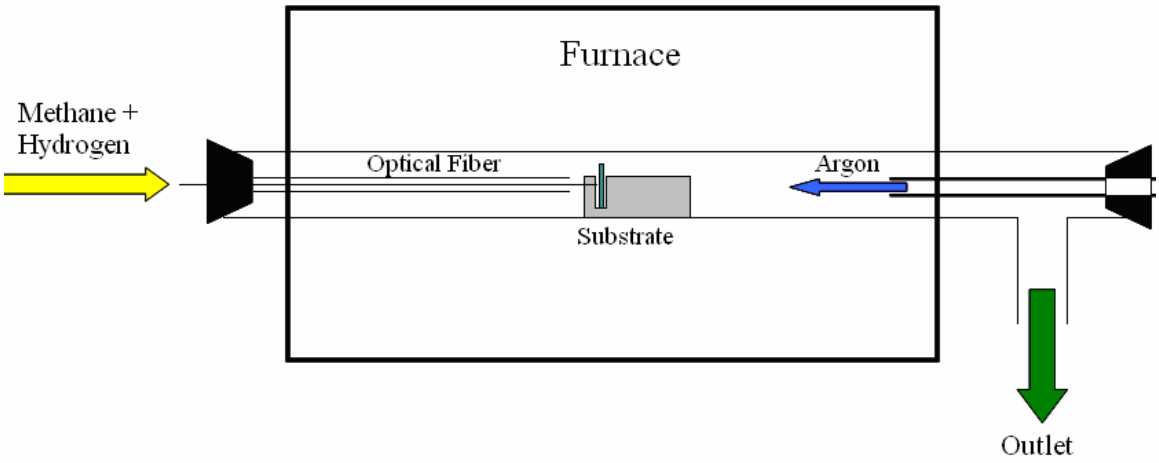

Figure 12
Schematic diagram of the apparatus used for the optical fiber experiment

It is important to notice that while both the hydrogen and the methane were flowed (separately) through the optical fiber, the argon was flowed from the other (outlet) end of the furnace because the maximum flow rate through the fiber was severely limited.

An initial experiment to grow nanotubes *inside* of the optical fiber was performed in which alumina supported iron catalyst was deposited by dipping the fiber tip into catalyst solution and allowing capillary forces to draw catalyst inside the fiber. We then flowed methane through the fiber as depicted in figure 12 except without the substrate present. Imaging the optical fiber in the SEM was difficult due to charging, but sputter

coating a conductive film onto the sample allowed us to verify the lack of significant nanotube growth inside or on the tip of the optical fiber.

Next, we tried growing nanotubes on a silicon substrate by flowing gas through the fiber, this time with the catalyst deposited on the substrate rather than inside the fiber (Figure 12). Before attempting this experiment, we performed a rough calibration of the maximum flow achievable through the optical fiber. An estimation of this flow rate was attained by setting the regulator to its minimum readable setting and submerging the optical fiber in water. We then counted the number of bubbles emerging in a given time interval, and approximated the size of the bubbles to estimate the maximum flow rate at about 0.1 SCCM. Achieving precise control over this flow rate proved extremely difficult using the course flow controllers at our disposal, so we assume for this experiment only two discrete flow states for the fiber: 0 and 0.1 SCCM. A naïve approximation of the average flow velocity inside the tube gives an approximate flow of 0.2 m/s inside the fiber. This number should be compared with the velocity obtained in a control CVD experiment where typically about 1 SLM of methane is flowed through a tube 1 inch in diameter, giving roughly an identical average flow velocity of 0.2 m/s.

These experiments proceeded very much like normal CVD nanotube growths with the gas flow confined inside the optical fiber rather than dispersed throughout the whole furnace tube (see Section 6 for more details). A typical alumina supported iron catalyst was deposited in solution onto a silicon substrate which was then placed in the center of the furnace inside of a quartz chip holder. The chip holder maintained the substrate in a vertical orientation (normal to the optical fiber) at a distance between ~ 0.5 mm and ~ 5 mm from the tip of the optical fiber. Approximately 700 SCCM of argon was flowed

from the rear of the furnace while it was heated to 980 ^{o}C. At this point, the hydrogen flow through the fiber was turned on for five minutes (with an assumed flow rate of ~0.1 SCCM). The hydrogen flow was then shut off, followed by 10 minutes of CH_4 flow at the same rate.

This experiment was attempted a number of times and proved to be unsuccessful for a variety of reasons. One important flaw in the experimental setup was that even slight increases in the gas pressure applied to the upstream end of the optical fiber would cause the o-ring around the furnace tube to slip. This was clearly due to the fact that we did not have sufficient control over the gas flow entering the fiber (the lowest pressure we could reliably apply to the fiber was too high). This lack of flow rate control also prevented us from meaningfully investigating flow rates above or below the nominal 'maximum' flow rate of 0.1 SCCM.

Careful SEM imaging of the samples revealed that none of them had any nanotube growth, and many of the samples showed signs of amorphous carbon deposition (Figure 13).

a)

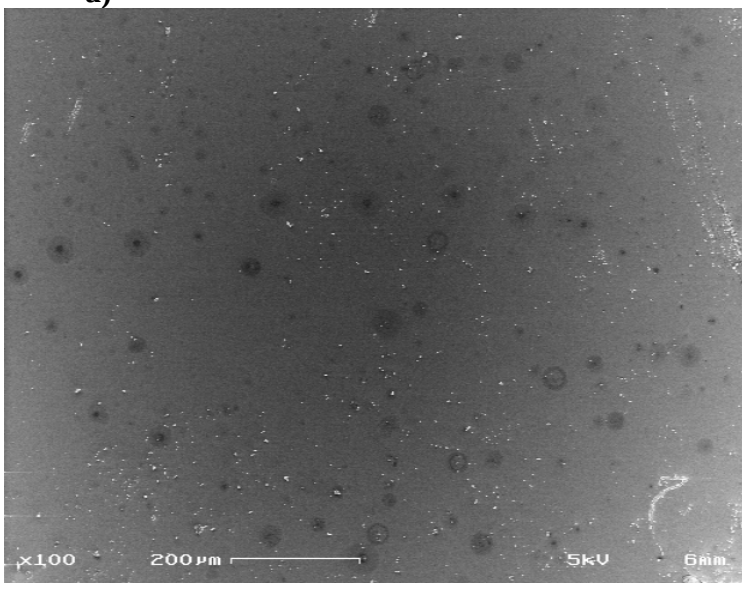

b)

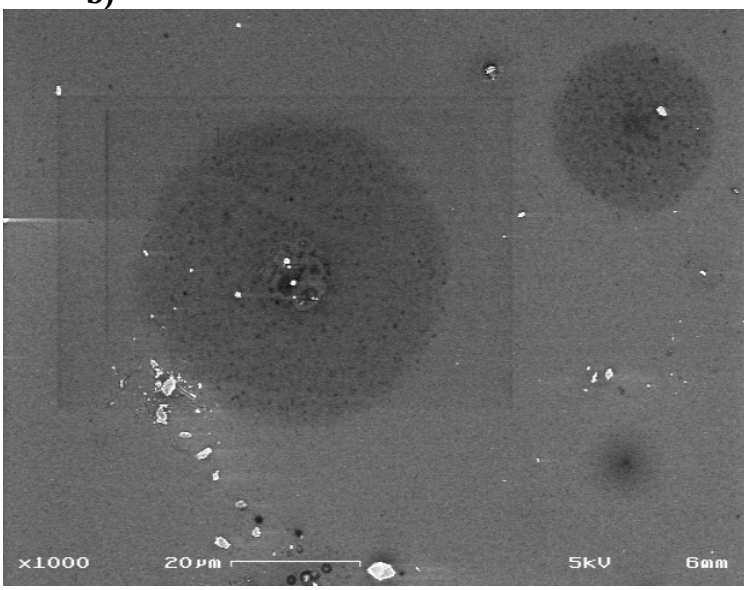

Figure 13
a) *SEM image of substrate used in CVD run with gas flowing through the hollow-core optical fiber where dark circles are likely regions of carbon deposition* **b)** *closeup of dark regions..*

Considering that some (but not all) of our experiments resulted in the inside of the furnace tube being coated with similar amorphous carbon deposits it would have been especially interesting to explore the possibility that either the local methane pressures, or the methane flow velocities inside the furnace tube were too high. This problem could presumably be resolved by installing accurate low-flow controllers, however we opted to increase the effective diameter of the fiber by using a quartz nozzle instead.

Another problem with this experiment was that it was extremely difficult to keep track of the location on the substrate at which the fiber was 'aiming.' We could keep track of this orientation to within a couple of millimeters by aligning the chip so that the fiber was pointing at certain reference markings, however this poor spatial resolution proved limiting when it came to imaging the substrates. It is doubtful that this issue was critical, however, because extensive imaging of the substrates showed not only a general

lack of nanotubes, but also substantial spatial uniformity in the patterns of amorphous carbon deposition suggesting that any potential nanotube growth would not likely be confined in a particular region of the substrate.

This technique would have potentially allowed directed growth of nanotubes by targeted delivery of source gas (Section 3.3.3). As previously mentioned, we have reason to believe that one significant problem with this experiment was our lack of control over (or accurate knowledge of) the flow rates through the fiber. Because of this, we adapted this experiment to use a quartz nozzle with a significantly larger aperture, along with accurate low-flow flow controllers, to attempt to further explore the issues presented by this initial experiment.

6. Experimental Setup

6.1. CVD Chamber

The primary apparatus for running the present experiment is a chemical vapor deposition chamber consisting of a 38 cm furnace (Linberg/ Blue M Model TF55035A-1) with a maximum temperature of 1100 ^{o}C, inside of which runs a four foot length of 1 inch quartz tube (Figure 14). Compressed gas cylinders of methane, hydrogen, and argon connected to calibrated flowmeters allowed the controlled flow of the requisite gases through the CVD chamber. Argon gas was metered using a Gilmont N092-04 flowmeter, hydrogen with a Gilmont 02281 flowmeter, and methane with an Aalborg 042-15-ST flowmeter. The outflow was passed through two beakers, one of which was filled with mineral oil to prevent backflow of any unwanted gas, and the other was empty and acted as a safeguard against the backflow of oil into the CVD chamber itself. From the beakers the gas was then channeled into a fume hood.

Figure 14
Photograph of CVD furnace, gas flow controllers, and compressed gas cylinders.

The nozzle was added as a modification to this traditional CVD setup. There were two different nozzles implemented in this experiment, both of which were custom made out of ½ inch quartz tubing (Space Glass, Inc.), having apertures of 700 um and 2.4mm. The methane and hydrogen were then flowed through the ½ inch nozzle tubing, with the nozzle tip located approximately at the center of the furnace, vertically centered by 3 quartz supports affixed to the ½ inch tube near the nozzle. The nozzle flow was then normally incident on the substrate which was held at a variable distance by a quartz chip holder (also custom made by Space Glass, Inc.). The chip holder consisted of a trench into which the nozzle tip would slide, a thin slit (~ 1 mm wide) to hold the chip vertically, and a handle with which to slide the chip holder in and out of the furnace using a quartz hook attached to a dowel (Figure 15).

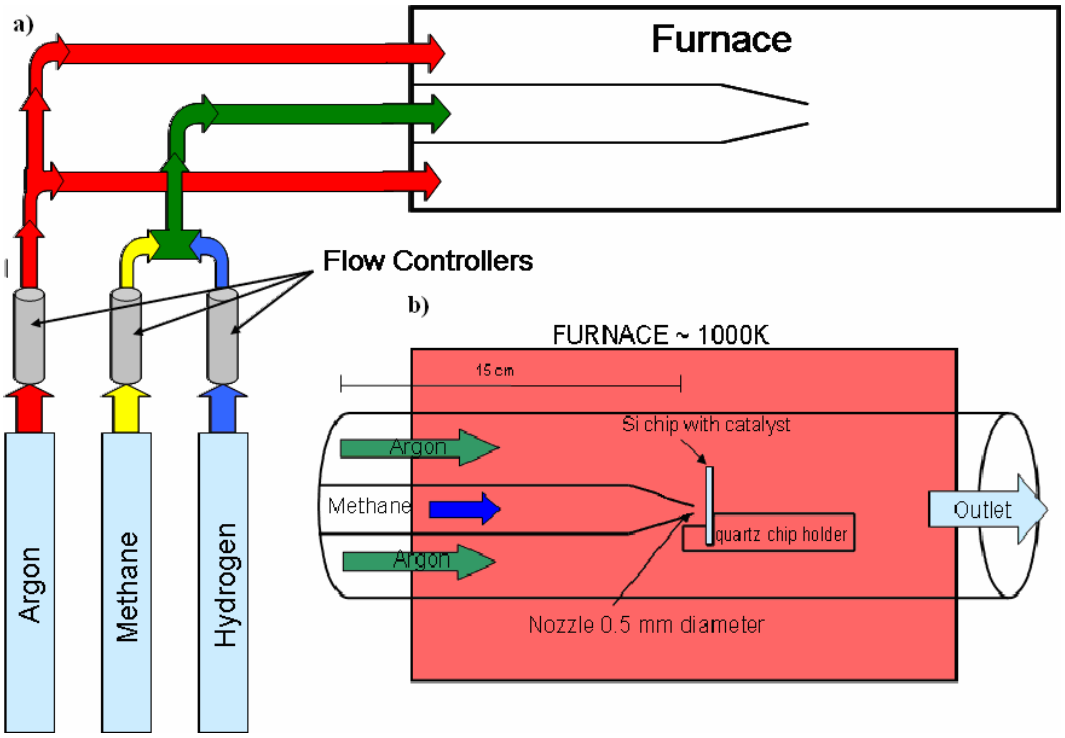

c)

Figure 15

Schematic diagram depicting the nozzle CVD apparatus. ***a)*** *shows the gas flows and flow controllers while* ***b****) shows the main components of the apparatus including the nozzle, furnace tube, substrate, and chip holder.* ***c)*** *Photograph of the 0.7 mm nozzle aligned with a Si substrate in the quartz chip holder.*

6.2. Catalyst Deposition

Two different techniques for depositing iron catalyst were employed in this experiment: depositing in solution and evaporating iron onto the substrate. In both cases the substrates used were silicon chips cut from 4 inch wafers having 200 nm SiO_2 layers. Depositions from solution were performed using an iron catalyst solution prepared by combining 20 mg Iron (III) Nitrate Nonahydrate (Aldrich Chemicals) with 5 mg Bis(acetylacetonato) – dioxymolebdenum(VI) (Aldrich Chemicals), and 15 mg alumina (Degussa) in 15 mL of methanol. These solutions were stirred overnight when first made, and were stirred for 30 minutes and sonicated for 30 minutes (using a Branson 2200 sonicator) prior to each usage. Approximately 5 drops of solution were then pipetted onto the substrate followed quickly by blow-drying.

Thin film catalyst depositions were performed inside a home-made evaporation chamber (Figure 16). The chamber consisted of a bell jar which was evacuated first by a roughing pump, then by a cryopump to pressures in the 10^{-6} torr range.

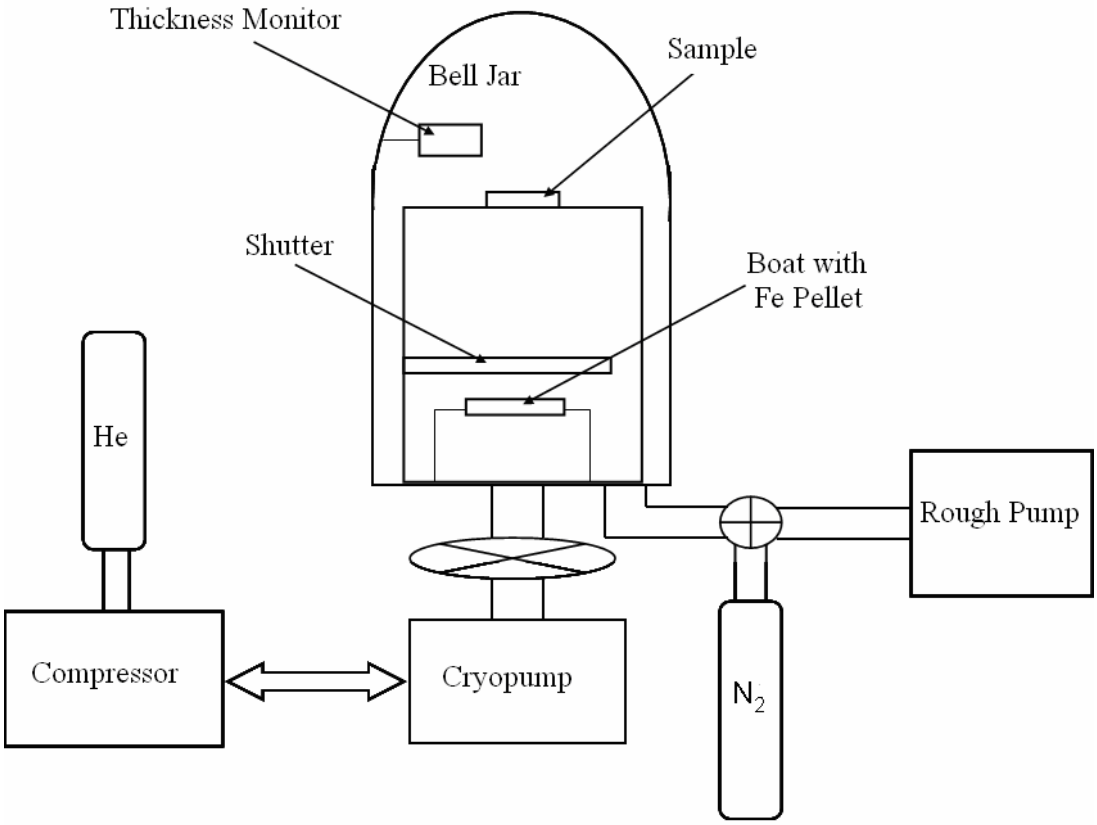

Figure 16
Schematic diagram of the evaporation chamber apparatus.

High-purity (99.95%) iron pellets (Kurt J. Lesker Co.) were then placed inside tungsten boats and ~ 170 A of current was passed through the boats to melt the iron. We used evaporation masks consisting of a grid of 3 mm circular holes fitted with TEM grids (Ted Pella, Inc.). The TEM grids had 500 μm square openings separated by a 100 μm thick copper grid, allowing depositions of 3 mm diameter circles of 500 μm square catalyst pads (Figure 17). The deposition thickness was monitored using a crystal thickness monitor, and a moveable shutter allowed control over this thickness of the depositions. Most of the work in making the thin-film evaporation technique operational for nanotube growth was done by Elias Penilla (Penilla, 2006).

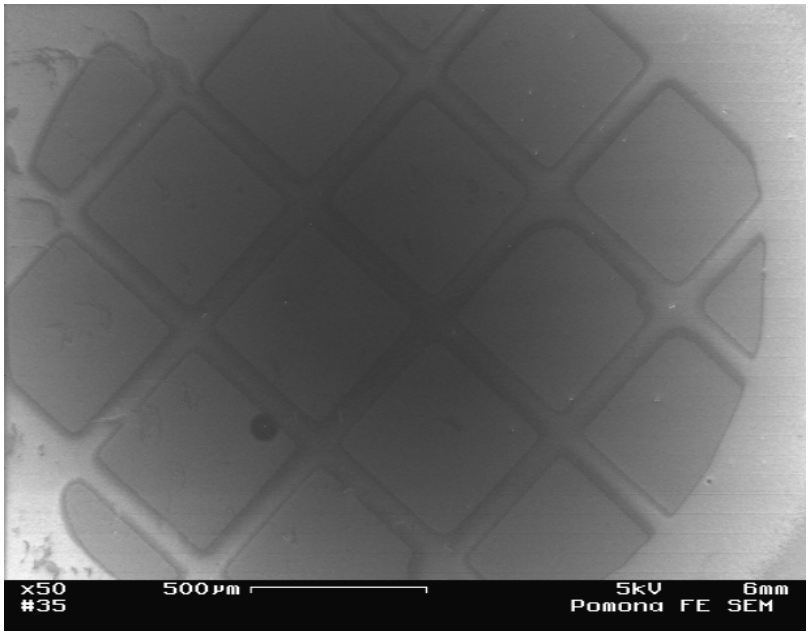

Figure 17
SEM image showing the 3 mm TEM mask containing a grid of 500 µm catalyst pads.

6.3. Procedure

For both of our nozzles, a similar range of flow rates was explored that extended from about 5 SCCM to around 1650 SCCM. In both cases the same quartz chip holder was used to position the chip about 1 – 4 mm from the nozzle in the 0.7 mm nozzle case and about 1 cm from the nozzle in the 2.4 mm case. The location of the impinging gas stream was centrally fixed relative to reference scratches made on each of three edges of the substrate. Although this positioning technique allowed a rough determination of the location of the gas stream, precise positioning of the substrate inside of the furnace was difficult and probably only accurate to within a couple millimeters.

Once the substrate was properly positioned inside of the furnace, the furnace was heated to 1000 ^{o}C while argon was flowed around the outside of the nozzle tube (Figure 15). We then flowed hydrogen followed by methane, both through the nozzle. The

specific flow rates of hydrogen and methane were varied from experiment to experiment as well as the duration for which each gas was flowed. Also, in some experiments the hydrogen flow was turned off before the methane flow was initiated while in others both gases were flowed simultaneously. In general, when using the solution based catalyst, the hydrogen was flowed for ~ 10 minutes and then was turned off while methane was flowed for ~ 10 minutes. For the evaporated catalyst, hydrogen was typically flowed for ~ 5 minutes before methane was added and both gases were flowed together for ~ 15 minutes, these procedures being generally established in previous experimental work (Ferguson, 2003 and Penilla, 2006).

All runs with the 0.7 mm nozzle were performed on samples that had catalyst deposited in solution. For the runs with the 2.4 mm nozzle some of the samples had solution based catalyst while others had evaporated catalyst. Imaging of the samples was performed using a Leo 982 Field Emission Scanning Electron Microscope (FE-SEM).

6.4. Control Samples

Throughout the course of this experiment, a number of control experiments were performed. For these samples the catalyst deposition procedure was identical, and the actual growth conditions were maintained as close as possible to the experimental conditions. Samples were placed in the furnace (heated to 1000 ^{o}C) where all the relevant CVD gases were flown throughout the entire furnace tube (rather than through a nozzle), with the substrate oriented horizontally (tangent to the gas flow). The gas flow procedure was as follows: first 180 SCCM of H_2 was flowed for 5 minutes, followed by 10 minutes of CH_4 flow at 1650 SCCM (1 SLM of argon flowed throughout the growth).

Successful nanotube growth, even under control conditions, has not been totally consistent, however we believe that we have achieved an effective 'recipe' for the solution based catalyst which has consistently yielded nanotubes. One observation of our control samples that will be important in our later discussion (Section 9) is that in nearly all cases there is a substantial density of alumina clusters in which to search for nanotubes. We estimate that on average (out of 8 control samples) there was about 1 large ($d \geq 1$ μm) alumina cluster per 10 μm^2. This number varied somewhat due to uneven drying of the catalyst solution, but in all of the control samples (with the newer catalyst recipe) the alumina distribution was fairly uniform (Figure 18). Variations in alumina distribution due to slight differences in the age of the catalyst or in stirring or sonication times did not seem to be significant.

a)

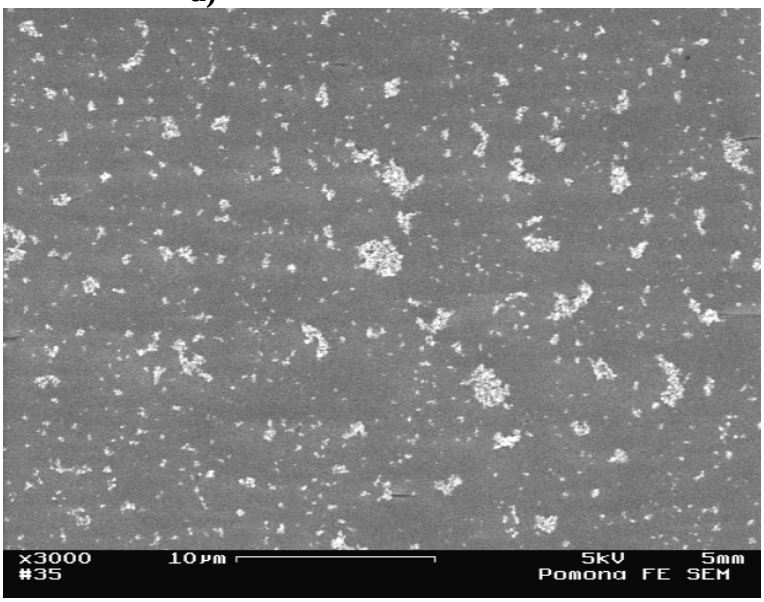

b)

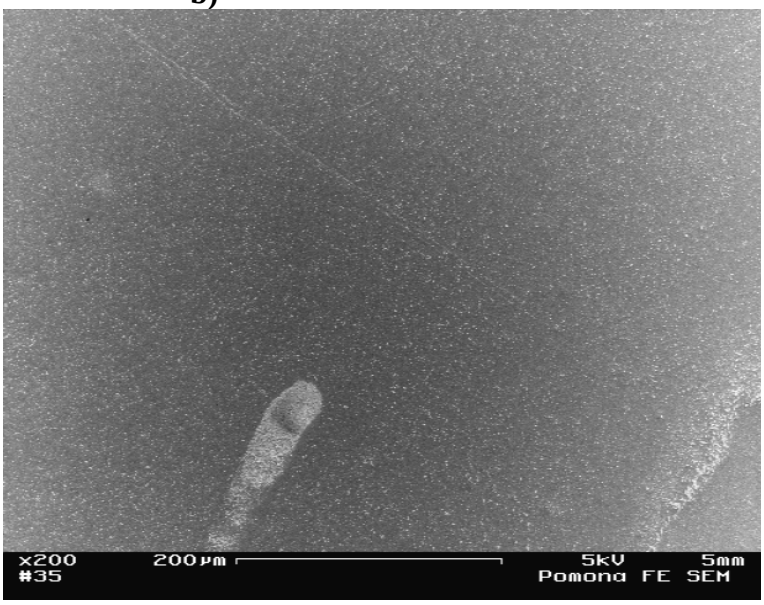

Figure 18
SEM images of control samples indicating **a)** *a typical local density of alumina clusters and* **b)** *an estimation of the uniformity of this distribution over macroscopic scales.*

Also of importance was the fact that in every control sample grown with the 'newer' catalyst recipe, we easily found single-walled nanotube growth in almost every large ($d \geq 1$ μm) alumina cluster, as well as in many of the smaller clusters. The catalyst particles themselves appeared to be largely confined to the alumina clusters so we do not find significant nanotube growth outside of the alumina clusters. Typical densities of nanotubes found inside of the alumina clusters were around 10 nanotubes/μm^2, with extremely high densities of nanotubes being found in large ($d \geq 10$ μm) alumina clusters (Figure 19).

a)

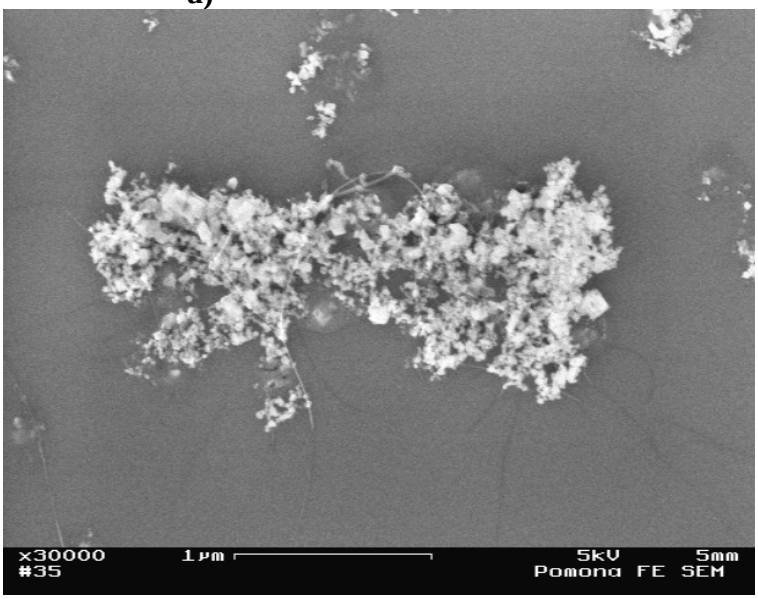

b)

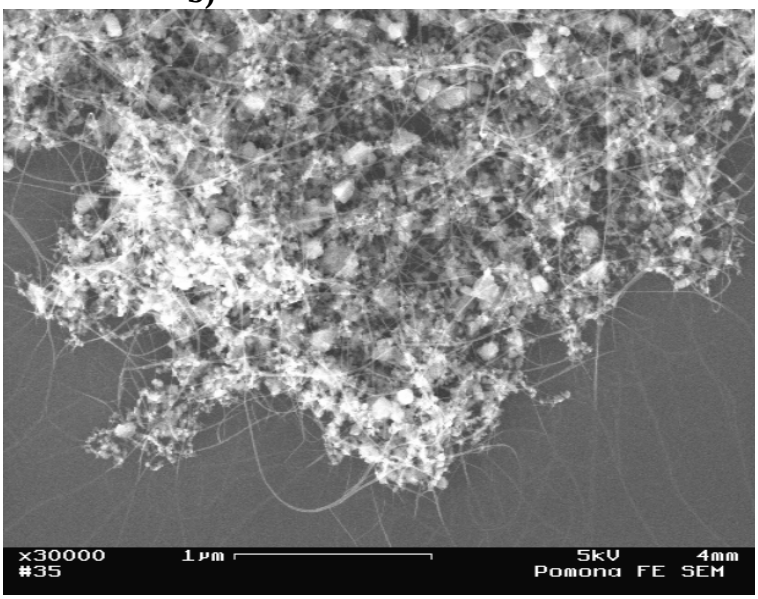

Figure 19

SEM images showing **a)** *average nanotube growth in a typical ~ 1 μm^2 alumina cluster and* **b)** *high nanotube densities in very large alumina clusters.*

7. Results

7.1. 0.7 mm Nozzle

We attempted to grow nanotubes using the 0.7 mm nozzle in a series of experiments which were largely identical except for variations in the methane flow rate. Although none of our experiments showed significant nanotube growth, imaging the substrates did provide clues as to factors that might have prevented nanotube formation.

7.1.1. Carbon Deposition

One immediately apparent finding of these experiments was that any growth run with the 0.7 mm nozzle using a methane flow rate greater than ~ 50 SCCM left the nozzle coated with a silver layer of carbon (for the 2.4 mm nozzle carbon depositions were actually seen on the nozzle at even lower flow rates). Similar amorphous carbon depositions have been observed on quartz tubes in previous CVD experiments using ethylene as the source gas (Hata et al., 2004). In higher flow cases, this deposition actually extended onto the sample holder as well as the furnace tube itself.

Another important observation was that samples grown with the nozzle exhibited dark splotching patterns, which we believe to be indicative of amorphous carbon deposition. These depositions tended to cover (to varying degrees) most of those samples grown with high (> 50 SCCM) methane flow rates (Figure 20), although no direct correlation could be made between the extent of the deposition and the flow rate.

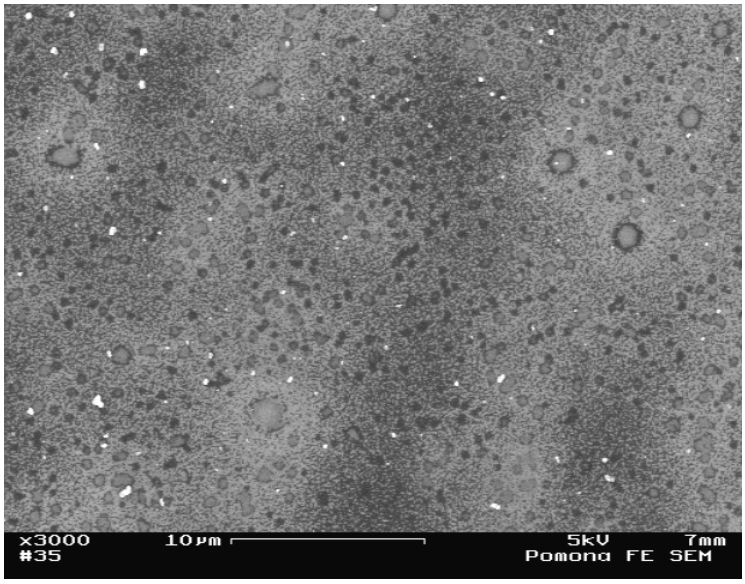

Figure 20
SEM images of splotching patterns for sample grown with methane flow rates of 98 SCCM.

These dark splotches are also found to a much lesser extent on the control samples (as mentioned in Section 5.2, the specific catalyst/source gas combination we are implementing does produce some amorphous carbon).

Additionally, there seemed to be a general lack of visible alumina clusters in which to look for the tubes when imaging with the SEM (recalling that in control experiments, nanotubes would grow from catalyst particles largely embedded in clusters of alumina support). Although the distribution of alumina on the control samples was not totally uniform from sample to sample, almost all control experiments showed significantly higher alumina densities (Section 6.4). Given this, there seem to be two potential explanations for the lack of visible alumina on these samples: 1) the alumina was 'blown' off the surface by gas flow coming from the nozzle, or 2) imaging of the alumina was obstructed by a carbonaceous layer deposited during the growth.

Considering that the alumina is bound to the surface strongly enough to withstand the far more substantial air flows associated with the blow drying process, these results suggest that the second explanation is far more likely. Accordingly, this reinforces our belief that the dark splotch patterns are indicative of extensive amorphous carbon deposition, occurring to varying degrees for all of the nozzle experiments we ran. Confusingly, however, even the experiments with extremely low (< 10 SCCM) methane flow rates showed a somewhat reduced density of visible alumina clusters, indicating that obscuring amorphous carbon layers were forming even in these cases (these issues will be further discussed in Section 9). It should be noted, however, that on some of the low-flow samples (as well as near the edges of some samples with higher flow rates) unobstructed alumina clusters were found, however there were no nanotubes in the clusters. Once again, the precise nature of the relationship between the amount of visible alumina and the flow rates used proved difficult to quantify given our sample size.

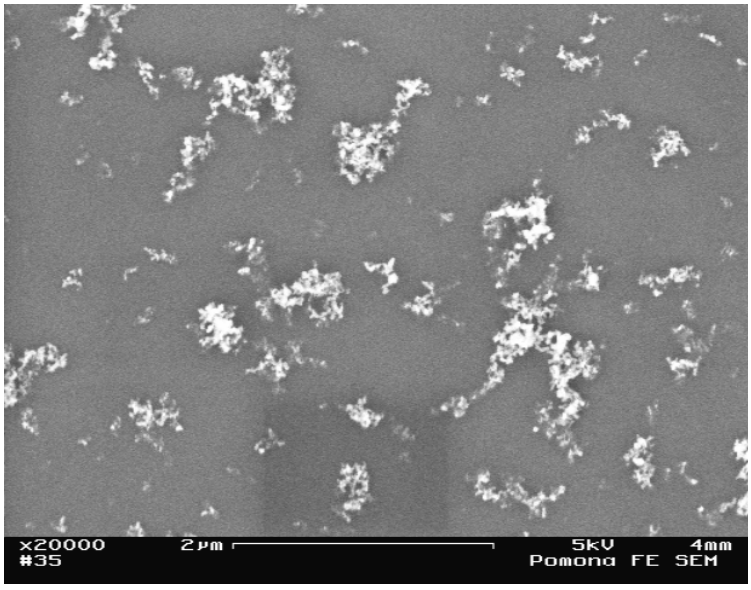

Figure 21
SEM image of a sample grown with a methane flow rate of 7 SCCM showing apparently unobstructed alumina clusters.

7.1.2. Local Nanotube Growth

Interestingly, a small, extremely local collection of nanotubes was found less than 1 mm from the edge of the chip grown with a flow rate of 680 SCCM (Figure 22).

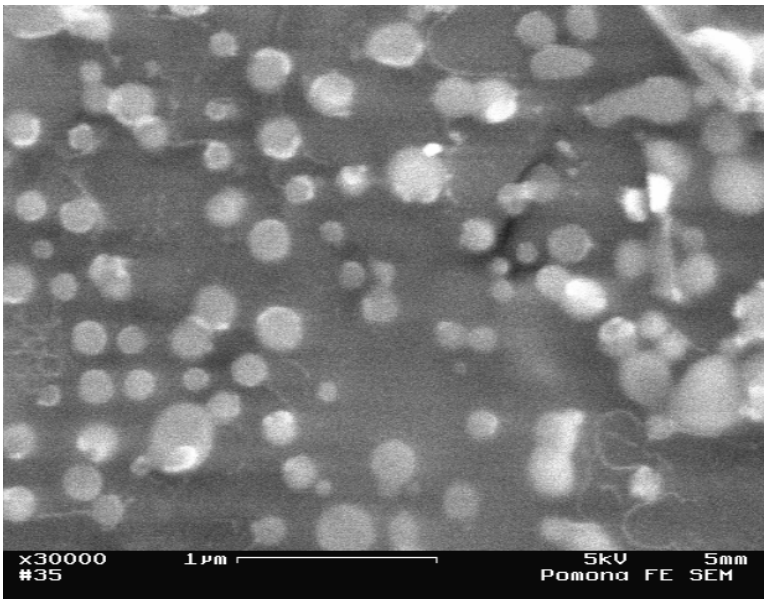

Figure 22
SEM image of nanotubes that were found on the edge of the sample grown with a methane flow rate of 680 SCCM.

Other isolated individual nanotubes were found on several occasions on other samples, however this was the only instance of an area of consistent nanotube growth. Possible explanations for this will be explored in Section 9, but the fact that tubes were only found at the edge of the chip where methane pressures would be lowest initially suggested that appropriate growth conditions could be achieved using some flow rate < 680 SCCM.

7.1.3. Catalyst Poisoning

"Catalyst poisoning" is a process whereby the catalyst particles become overwhelmed by surface carbon deposition, becoming inactivated with respect to nanotube growth (Section 3.4.1). To test the possibility that the catalyst was becoming

poisoned during these experiments we took two samples that had been used in nozzle growths with flow rates of 5 SCCM and 98 SCCM and put them back into the furnace for a second growth without the nozzle (under control conditions). After the second growth, only the chip that had been grown under the lower nozzle flow conditions (5 SCCM) showed any nanotubes, and even then the nanotubes were only found in one location out of many scanned (Figure 23).

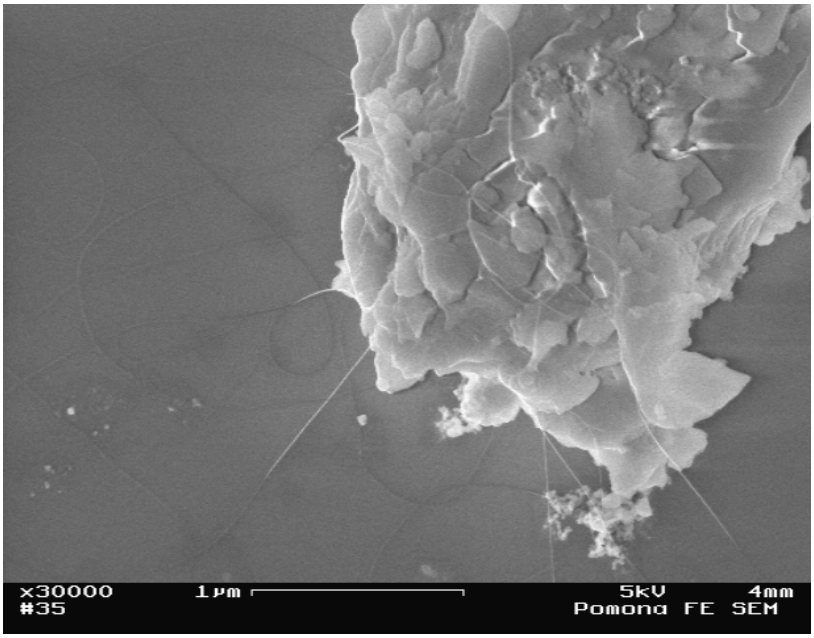

Figure 23
SEM image of nanotubes found after a second growth (without the nozzle). The original methane flow rate with the nozzle was 5 SCCM in this case.

Although there were likely other locations with nanotube growth, they were certainly more sparsely distributed than in the normal control growths. The sample previously used in the 98 SCCM nozzle flow experiment showed no nanotube growth at all. It is worth noting that even though both samples showed fewer alumina clusters after the original nozzle growths, there were still regions of visible alumina clusters in both samples which failed to grow nanotubes during the attempted re-growth.

A final attempt was made to search for the region in flow rate parameter space (whose existence was implied by the nanotubes found on the edge of the previously mentioned chip) by varying the methane flow rate from 5 – 100 SCCM over the course of a growth. The flow rate was increased by increments of ~ 10 SCCM, holding for ~ 1 minute at each flow rate. Extensive imaging of this chip showed no signs of nanotube growth, however there did not seem to be as extensive of a carbon deposition as in the 100 SCCM flow case (as determined by the density and appearance of the alumina clusters) (Figure 24). This preliminary result suggests that this sample may not have been exposed to the high flow conditions long enough to develop as extensive of a carbon deposition, however further work will be required to determine the flow-dependant carbon deposition rate.

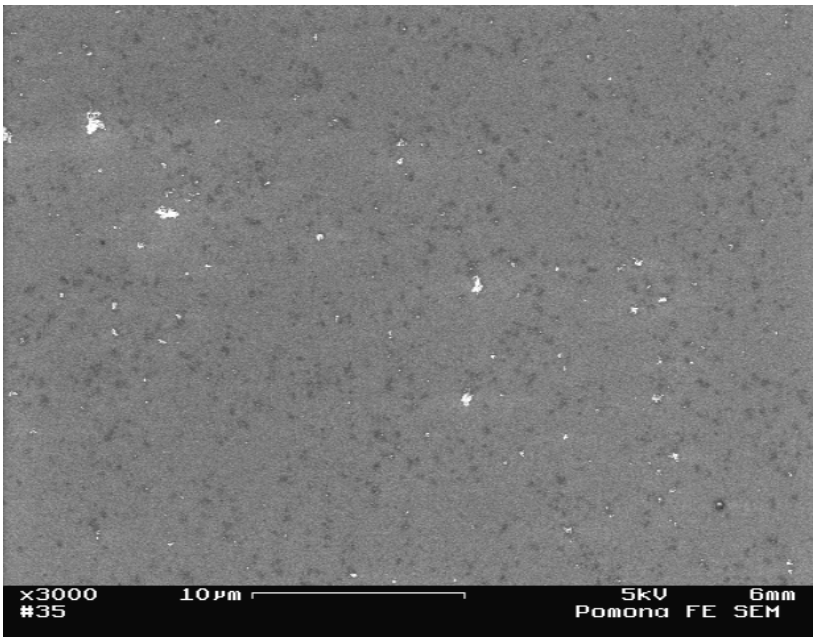

Figure 24
SEM image of black splotches found when varying the flow rate from 5 SCCM to 100 SCCM during the growth process.

7.2. 2.4 mm Nozzle

7.2.1. Solution-Based Catalyst

The results obtained with the 2.4 mm nozzle were qualitatively very similar to those in the 0.7 mm case. The same carbonaceous coatings of the nozzle (and in some cases the chip holder as well) were found, although this time the coatings occurred for flow rates as low as 20 SCCM. Again, the existence of amorphous carbon layers deposited on the substrates themselves showed a tight correlation with the existence and the extent of the coating on the nozzle.

A few nanotubes were found on the sample grown with a flow rate of 1160 SCCM, although the chip was extremely dirty from the excessive carbon deposits (Figure 25).

a)

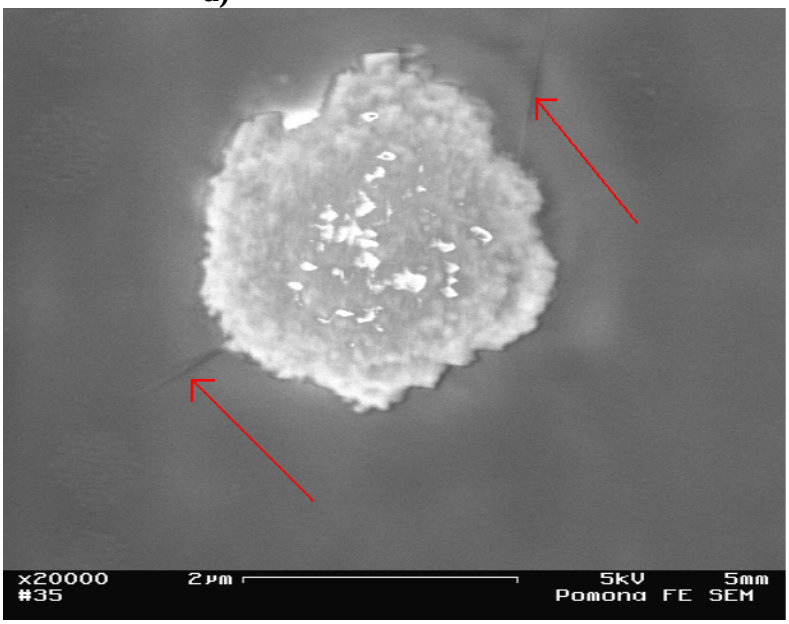

b)

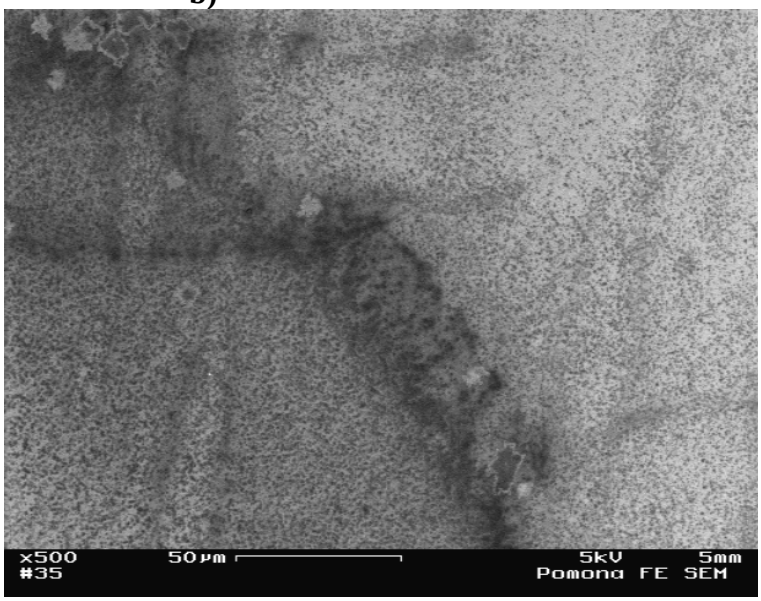

Figure 25
SEM images of sample grown with a methane flow rate of 1160 SCCM. **a)** *Shows one location were nanotubes were found.* **b)** *Shows the degree of carbon deposition covering the sample.*

It is worth noting that these nanotubes and the alumina cluster that they are growing outwards from have a hazy appearance (Figure 25a), seemingly covered with the suspected carbon layer.

7.2.2. Evaporated Catalyst

For the experiments using evaporated catalyst, we varied not only the methane flow rate, but also the thickness of the iron thin film deposition. From experiments without the nozzle, we have determined that the optimal thickness for growing nanotubes is around 8 angstroms, however growths that are somewhat thicker (up to around 15 angstroms) do show some nanotube growths as well (Penilla, 2006). Consistently achieving the desired film thickness initially proved difficult, and a number of the nozzle experiments were performed with thicker iron depositions simply due to experimental error.

Interestingly, for one such sample (a 15 angstrom deposition) to which we added 30 SCCM of methane through the nozzle, we found that not only was the nozzle tube coated with carbon, but the substrate itself was mostly covered with a yellow-orange coating (Figure 26a). Furthermore, when imaging the catalyst pads we noticed that many of them were covered with large blobs of carbon deposition several hundred microns across. Upon closer inspection, we found that these blobs had an abundance of MWNTs covering them (Figure 26b). The rest of the sample, including on and around catalyst pads that were not covered with these blobs, seemed to be devoid of nanotubes of any kind.

a)

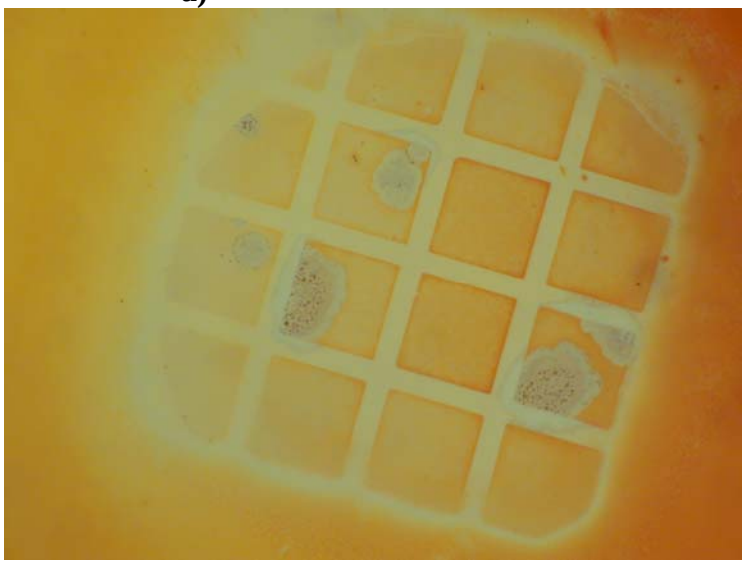

b)

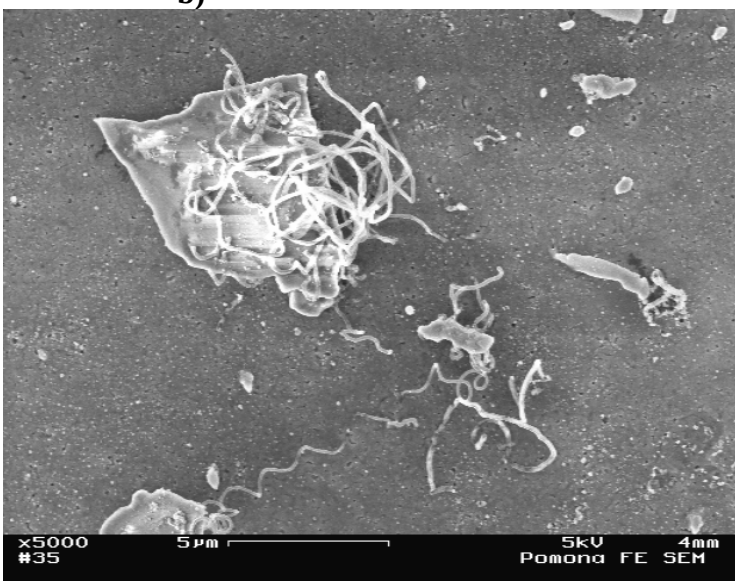

Figure 26
a) *Optical image showing the yellowish coating as well as the blobs of carbon deposited on some of the catalyst pads.* **b)** *SEM image showing many MWNTs scattered about on one of the aforementioned blobs.*

Because the carbon blobs seemed to indicate excessive methane present, this experiment was repeated several times with a lower flow rate of 20 SCCM (and thinner iron films ranging from 12 angstroms to the submonolayer ~6 angstrom regime). Of these lower flow experiments, only once did we find carbon blobs covering any of the catalyst pads, and we were unable to find any nanotubes (samples with identical catalyst thin films showed normal nanotube growth under control conditions). Instead, all three of the samples grown under these conditions had similar morphological features both on and around the catalyst pads, which appeared to be more than a monolayer thick. Most noticeable were sharp, linear formations that were probably indicative of thermal expansion in the underlying catalyst layer (Figure 27a).

a)

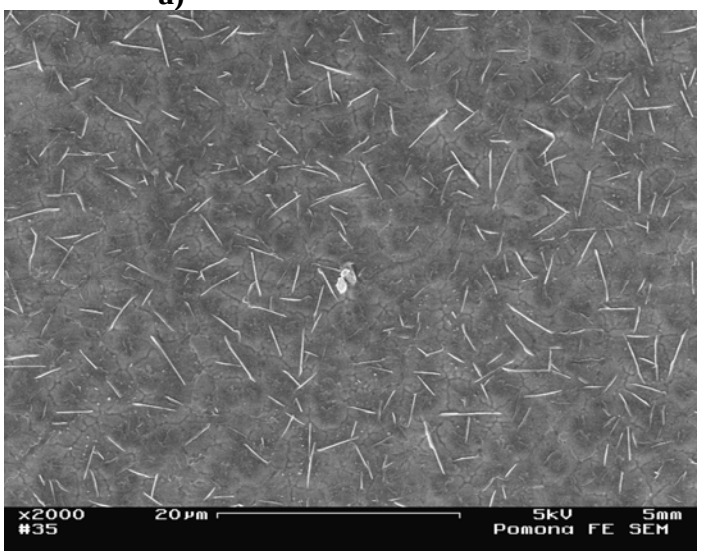

b)

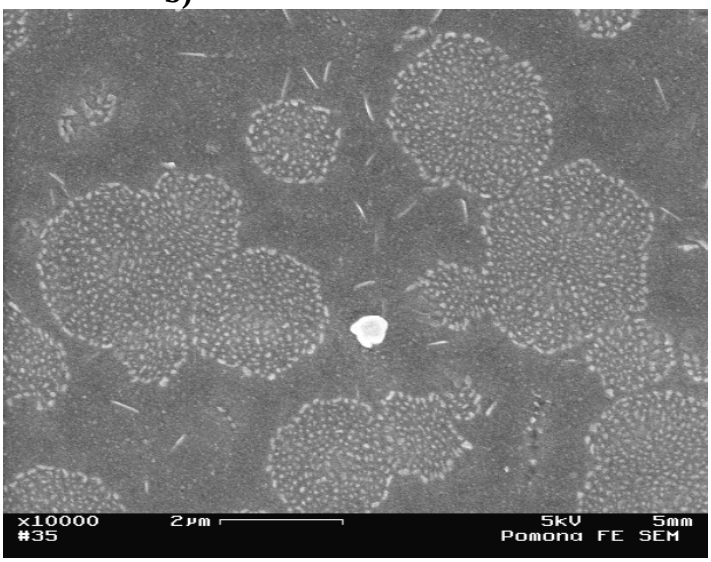

Figure 27
SEM images of sample grown with a 12 angstrom iron deposition and 20 SCCM methane flow. **a)** *Step edges on a catalyst pad* **b)** *Circular iron clusters.*

Also apparent on top of the catalyst pads were circular clusters of iron particles (Figure 27b). A reasonable explanation of these iron morphologies likely has to do with the presence and flow geometry of hydrogen (which is implicated in increasing catalyst mobility) (Section 3.3.2). Interestingly, we found that for all of our evaporated catalyst

samples with flow rates lower than 30 SCCM, there were no indications of excessive carbon decomposition. Not only were there no blobs of amorphous carbon forming on the catalyst pads in these cases, we didn't observe any 'obscuring' of the catalyst as with the alumina catalyst solution. This could be evidence that our speculations about the reason for observing lower alumina densities in nozzle growths are incorrect.

7.2.3. Chip Orientation

Because all of our control growths were run with the substrate surface oriented horizontally (tangent to the gas flow) whereas the nozzle experiments all had the chip oriented vertically (normal to the gas flow), a brief series of experiments was performed to determine if there were any 'substrate orientation' dependant effects on nanotube growth that could potentially explain the lack of tube growth in the nozzle experiments. These experiments were performed with two chips in the furnace during each growth. The horizontal (tangent) chip was placed upstream while the vertical (normal) chip was placed in the chip holder several centimeters downstream, creating enough distance between the chips that the flow-disruptive effects of the upstream chip would not be a consideration, while still keeping them close enough together to both be in the constant temperature region of the furnace (Figure 28).

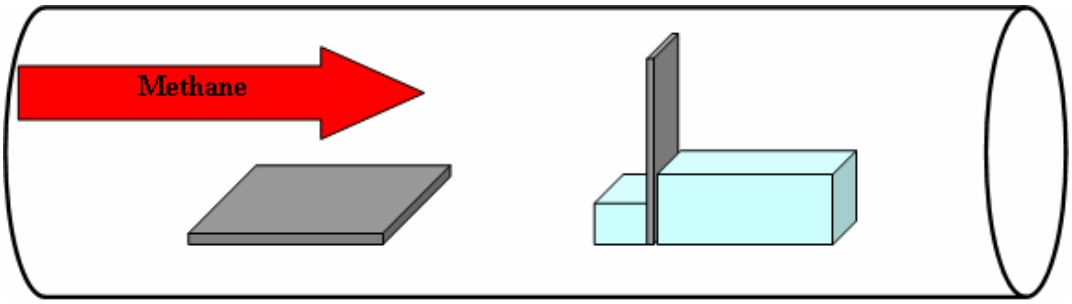

Figure 28
Schematic diagram of orientation experiments with the "tangent to flow" chip located upstream and the "normal to flow" chip located downstream.

The first of the experiments was run with a 1650 SCCM methane flow rate (the same as in a typical control run), and showed that there was no significant difference between the horizontally oriented control and the vertically oriented substrate (both grew substantial amounts of tubes). When the experiment was repeated with a 4630 SCCM flow rate, however, we found that the horizontally oriented chip grew nanotubes while the vertically oriented chip showed no nanotube growth at all (Figure 29).

a)

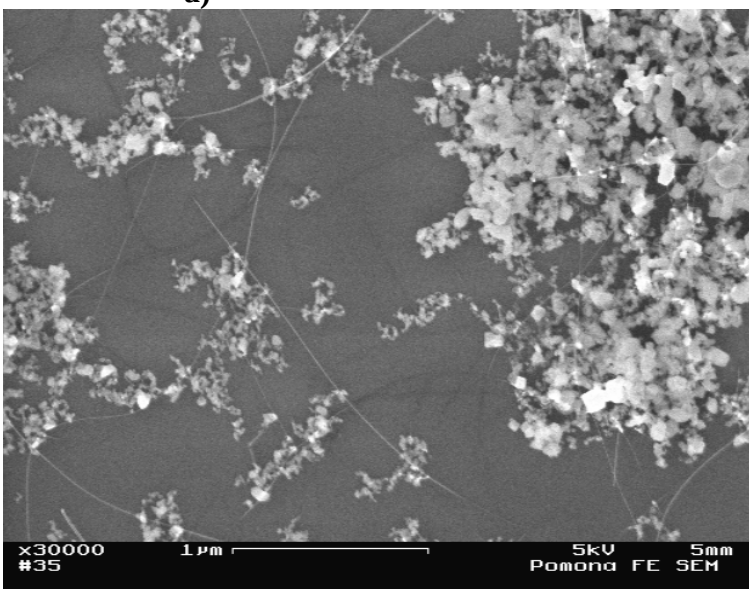

b)

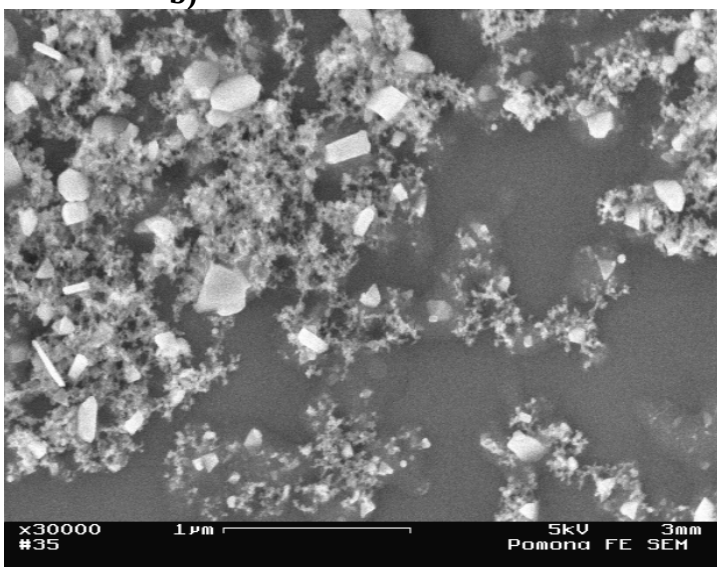

Figure 29
SEM images of **a)** *horizontally oriented* **b)** *vertically oriented chips grown with a 4630 SCCM methane flow rate showing* **a)** *tube growth and* **b)** *no tube growth.*

Of significant interest was the fact that, although the vertically oriented chip showed no nanotube growth, it did not show any of the signs of amorphous carbon deposition seen in the failed nozzle experiments. To test whether or not catalyst poisoning had still occurred in this case, the chip that showed no growth was put into the furnace a second time under control conditions (oriented tangent to the flow). We found that even under the control conditions the chip showed no tube growth, indicating that even though the carbon deposition was not visible, catalyst poisoning had still occurred.

A final experiment was run in which the 2.4 mm nozzle was used but where the chip was positioned tangent to the gas flow (without using the chip holder). In this case 90 SCCM was used with the gas stream approximately vertically level with the substrate. We found that this setup did not produce any nanotube growth, but also did not lead to any visible amorphous carbon deposition (similar to the case of the vertically oriented chip run without the nozzle). We assume that in this case the sample is showing catalyst

poisoning without enough carbon deposition to form a visible layer (as with the previous experiment).

8. Fluent Simulation

In order to better understand the gas flow and temperature distributions inside the experimental apparatus, a computational fluid dynamics (CFD) simulation was created using the Fluent 6.2.16 software package. As previously discussed, Fluent uses finite volume methods to solve the integral conservation equations associated with fluid flow, phase changes, heat transfer, and other physical processes, and provides an interface for postprocessing the data. For the simulation used in this work a number of limitations were encountered and several important simplifying assumptions were made. It will thus be important to clearly outline, and hopefully justify, these assumptions. In this section, I will outline the basic procedure used to make this simulation including creating the mesh, choosing appropriate models, and a presentation of the relevant results obtained.

8.1. Geometry and Meshing

The geometry and meshing for the simulation were performed using the CAD and meshing software package Gambit 2.2.30. For simplicity, the geometry implemented was two-dimensional (axially-symmetric about the centerline of the furnace), and only corresponded to a 16 cm length of the furnace tube centered at the midpoint of the furnace. This region corresponded to the length over which I took experimental data of the axial temperature profile, and easily contained all of the desired information. Because the furnace tube and the nozzle are both concentrically cylindrical, and because we hypothesize an approximately radially symmetric flow distribution at the surface of

the substrate, the asymmetries of the substrate and substrate holder (which are relatively minor) can safely be neglected as a first order approximation.

The geometry was created by defining all of the vertices individually and then connecting them with edges. To further simplify the model and to emphasize the processes at the substrate, the substrate holder was not included in the geometry and the substrate was modeled as a circular chip 1 cm in diameter and 0.5 mm thick. Due to the proximity of the nozzle to the substrate in the experimental apparatus (~1-2 mm), these assumptions should not have a dramatic effect on the fluid behavior at the surface of the chip, especially in the region immediately surrounding the point of incidence of the nozzle spray on the substrate. Figure 30 displays the initial geometry, indicating the dimensions of the edges.

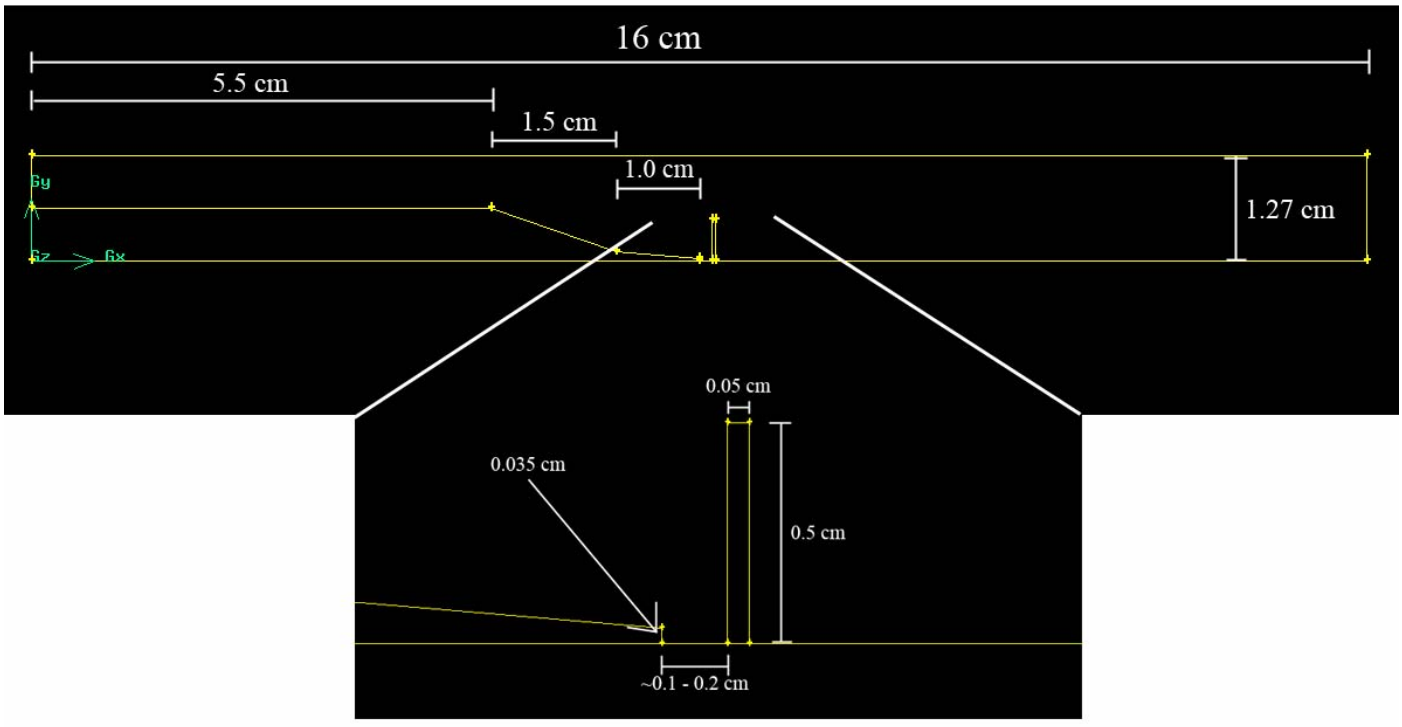

Figure 30
Diagram of unmeshed geometry indicating relevant dimensions.

Faces were then defined for each of the edges allowing the specification of functional 'continuum' types including the "inner fluid," "outer fluid" and "chip." These continuum types allowed material parameters to be defined uniquely for each region. The chip was identified as a solid continuum, the inner fluid was defined as the area enclosed by the nozzle, and the outer fluid constituted the remainder of the geometry (roughly corresponding to the initial separation between argon and methane flows). Boundary types were then defined including the walls, symmetry axis, fluid outlet, and separate fluid inlets for the methane and argon.

The next step was to mesh the geometry, and an initial attempt was made using Gambit's automatic meshing algorithm which defines nodes along the edges and creates a mesh for a given continuum region simultaneously based on a few simple user input parameters. The mesh created with this method consisted of about 135,000 elements and was overly fine in certain regions and too coarse near the chip, making it both slow and inaccurate where data was desired (Figure 31).

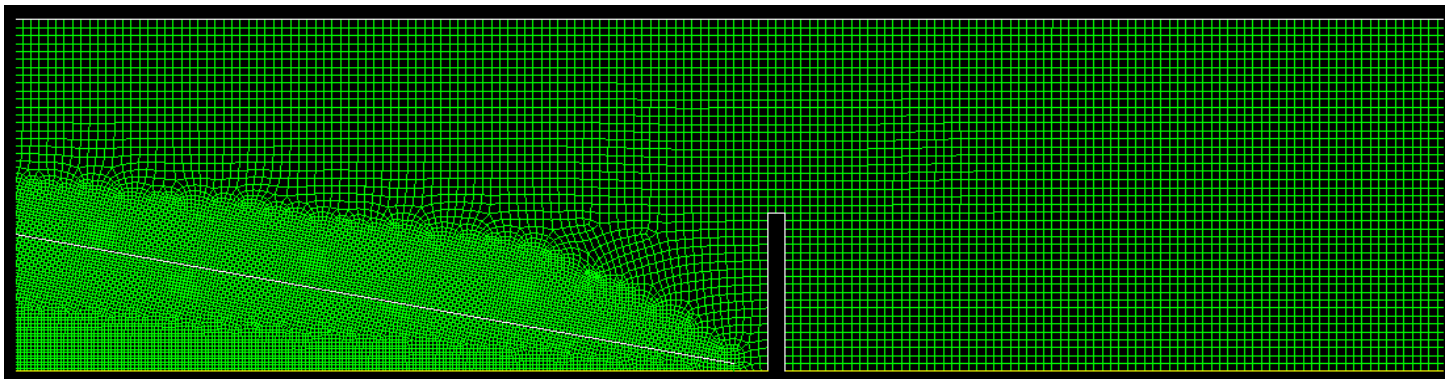

Figure 31

Central region of the initial meshed geometry as created in Gambit 2.2.30.

After several attempts were made at attaining initial results with this first mesh, an improved mesh was created by first defining the nodes along the edges and then meshing

according to the predefined nodes. Nodes were defined along each of the edges in such a way as to maximize the node density in the regions of interest (near the front face of the substrate). Thus, for a number of the edges a successive ratio was defined for the intervals between nodes, allowing node spacing to decrease geometrically towards the center of the apparatus. Typical node counts were on the order of 200 per edge. The three continuum regions were then independently meshed using the "Pave" method to create an unstructured grid of both quadrilateral and triangular mesh elements (Fluent, Inc.). This mesh consisted of only about 27,000 elements, much less than the previous mesh, and the concentration of elements around the substrate was significantly higher than the previous mesh (Figure 32). Thus, the second mesh was both more efficient and more accurate in the region of interest.

a)

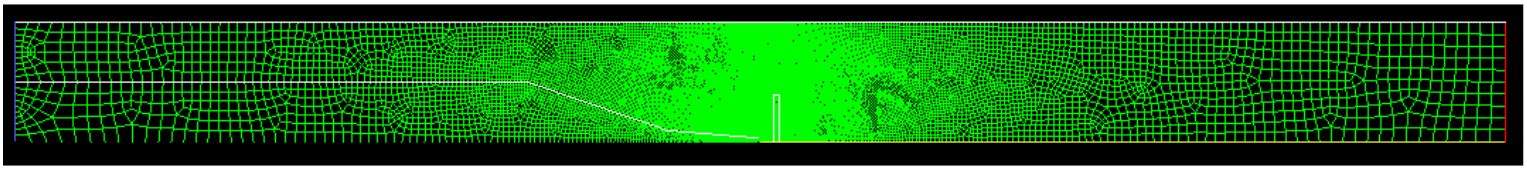

b)

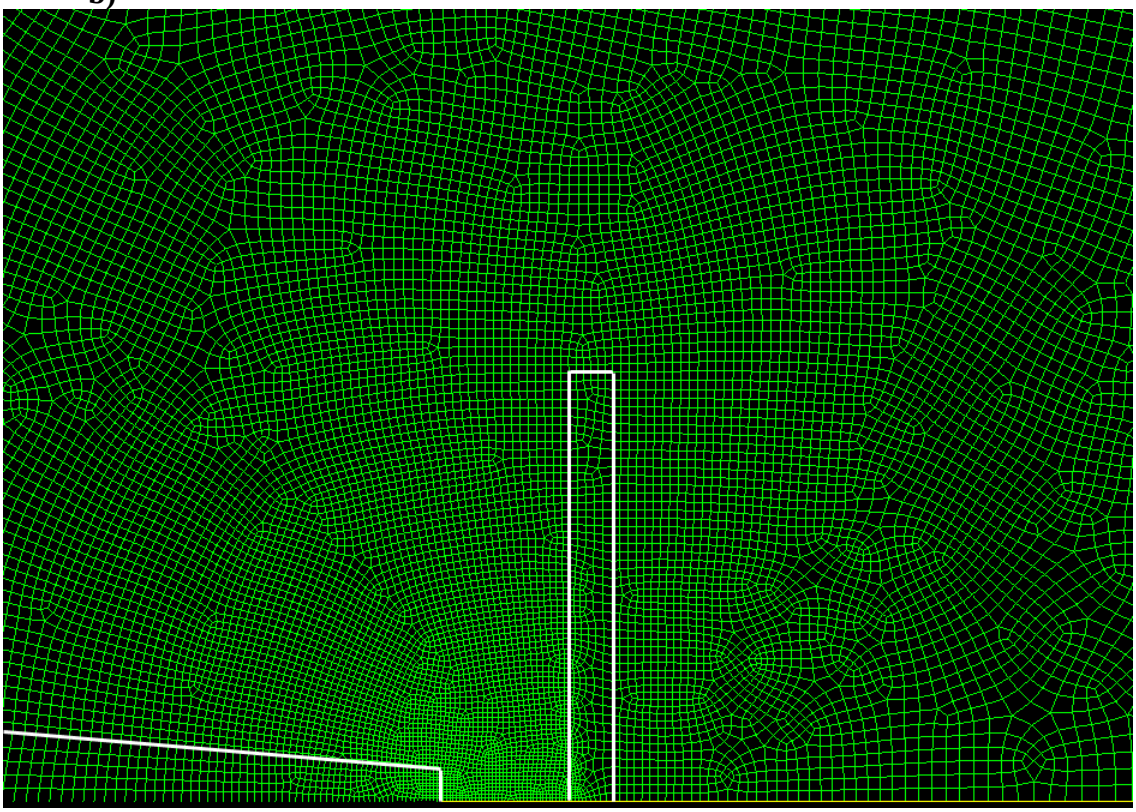

Figure 32
a) *Improved mesh* **b)** *Closeup of the central region.*

8.2. Choosing Simulation Parameters

In choosing appropriate settings for Fluent's numerical solver, computational accuracy was weighed against the desired degree of realism in the simulation. The solver employed was the 2D double precision model, and solved the governing integral equations (conservation of mass, momentum, and energy) in a segregated manner (one after another), checking for convergence after each iteration.

Although consideration of turbulence drastically increases the difficulty of the simulation, the geometry and Reynolds numbers associated with some of the experiments strongly suggest their consideration in some cases. For instance, a rough estimation of the Reynolds numbers of the flows involved in the simulation can be attained from

equation (2). Plugging in the characteristic velocities attained at the nozzle, along with a characteristic length associated with the geometry (the diameter of the nozzle, or the separation between the nozzle and chip) gives Reynolds numbers of roughly 400 and 40 in the high and low methane flow cases respectively. These numbers can easily be compared with values obtained in typical CVD experiments. For instance, if 1 SLM of methane is flowed through a furnace tube with a one inch diameter, the Reynolds number will be roughly 60. Furthermore, the Reynolds number of the flow inside the ½ inch nozzle tubing for the 100 SCCM case is about 25. These values clearly demonstrate that the flows associated with most CVD experiments are in the laminar regime ($Re < 100$).

Because the Reynolds number for the flow exiting the nozzle in the high flow case is substantially larger than 100 (Section 4), turbulence models were implemented to obtain time-dependant solutions for these cases. On the other hand, the Reynolds number associated with the low flow cases suggests that a laminar flow model (obtaining a time-independent solution) might be appropriate. While these approximations of the flow regime based on Reynolds numbers were crude, we found that the resultant velocity, pressure, and temperature profiles did not depend strongly on whether or not turbulence models were implemented, especially in the low flow case. Thus, in terms of the relevant results of the simulations, our choice of model (turbulent or laminar) was probably not critical.

For the high flow cases, the standard κ-ε turbulence model, a relatively simple model based on two equations, was selected for its "robustness, economy, and reasonable accuracy for a wide range of turbulent flows" (Fluent, Inc.). To decrease computation times, the general procedure was as follows: first the time-independent, laminar model

was used to reduce the residuals below a desired value (typically about 0.001), then the κ-ε turbulence model was turned on (still using the time-dependant solver) allowing the residuals to drop after which the time-dependant solver was allowed to run for enough time steps for the solution to converge below residuals of roughly 0.0001 or lower for all of the relevant parameters. A more complete listing of the model parameters that were chosen is given in Table 1.

Setting	**Selection Used**
Solver	Segregated
Space	Axisymmetric
Velocity Formulation	Absolute
Gradient Option	Cell-Based
Formulation	(Implicit)
Time	Steady/Unsteady
Porous Formulation	Superficial Velocity
Energy Equation	Yes
Viscous	Laminar/ κ-ε turbulence model
Radiation	Discrete Ordinates (DO)
Solidification/Melting	No
Argon Flow Rate	Varied
Methane Flow Rate	Varied
Argon/Methane Inlet Temp	1240 K
Backflow Temp	1260 K
Furnace Wall Temp	Temperature Profile From Experimental Data
κ-ε turbulence settings	Default
DO model settings	Default

Table 1

Listing of model parameters used in Fluent simulations.

The two materials used in the simulation were methane and quartz. Because hydrogen flows were usually performed prior to and separate from methane flows, they were ignored in the simulation. The physical properties of these materials as implemented in the simulation, including density, specific heat, thermal conductivity, viscosity, and absorption coefficient are listed in Table 2.

	Methane	Quartz(*)
Density (kg/m^3)	Incompressible ideal gas	2200
Specific Heat (J/K/kg))	2222	783
Thermal Conductivity (W/m/K)	0.0332	1.38
Absorption Coefficient (m^{-1})	N/A	0.001
Viscosity (kg/m/s)	1.087e-05	N/A
Internal Emissivity	N/A	0.93

Table 2

Listing of material properties used in Fluent simulations.
** http://www.mt-berlin.com/frames_cryst/descriptions/quartz%20.htm*

It is worth noting that incompressible flow was assumed because the gas flows in the simulation are all well below supersonic, and because temperature fluctuations were large the incompressible ideal gas model was used for the density of methane. The reference pressure (atmospheric pressure) was defined along the central axis at the downstream edge of the simulation.

Although Fluent is capable of handling multiple phases (e.g. fluid and particulate), it cannot represent the mixing of multiple fluids. Thus, it was not possible to model the flows of argon and methane at the same time, and thus "methane" was used to represent the flow of argon around the outside of the nozzle. The question of what methane flow rate to use to replace a given mass flow rate of argon was addressed differently depending on the information desired from each specific simulation. For instance, when flow velocity information was desired, the outer methane flow rate was typically adjusted to approximately equal the corresponding mass flow rate of argon. Because the viscosities of the two gases are within a factor of 2, we expect a reasonable qualitative approximation, although we must take care to treat with caution the precise numbers associated with the fluid flows given the large uncertainty of this assumption. Alternatively, when information about the temperature distribution at the substrate surface was desired, the substituting methane flow rate was set to match the heat flux

associated with the experimental argon flow rate (by adjusting for the difference in specific heats). Again, this assumption provided only a first order means for dealing with the inability to model multiple fluids simultaneously, however in most cases the flow parameters at the substrate should not be dramatically affected by these issues.

Since the temperature of the furnace was of critical importance to the model, the energy equation solver was used in the simulation. The temperature along the wall of the furnace tube (the outer boundary of the simulation) was determined by a 'profile' file (Figure 33) created according to the previously mentioned thermal couple experiment.

```
 ((temp-prof line 33)
(x
   0.00000E+00   0.50000E-02   1.00000E-02   1.50000E-02
   2.00000E-02   2.50000E-02   3.00000E-02   3.50000E-02
   4.00000E-02   4.50000E-02   5.00000E-02   5.50000E-02
   6.00000E-02   6.50000E-02   7.00000E-02   7.50000E-02
   8.00000E-02   8.50000E-02   9.00000E-02   9.50000E-02
   1.00000E-01   1.05000E-01   1.10000E-01   1.15000E-01
   1.20000E-01   1.25000E-01   1.30000E-01   1.35000E-01
   1.40000E-01   1.45000E-01   1.50000E-01   1.55000E-01
   1.60000E-01 )
(y
   1.27000E-02   1.27000E-02   1.27000E-02   1.27000E-02
   1.27000E-02   1.27000E-02   1.27000E-02   1.27000E-02
   1.27000E-02   1.27000E-02   1.27000E-02   1.27000E-02
   1.27000E-02   1.27000E-02   1.27000E-02   1.27000E-02
   1.27000E-02   1.27000E-02   1.27000E-02   1.27000E-02
   1.27000E-02   1.27000E-02   1.27000E-02   1.27000E-02
   1.27000E-02   1.27000E-02   1.27000E-02   1.27000E-02
   1.27000E-02   1.27000E-02   1.27000E-02   1.27000E-02
   1.27000E-02 )
(t
   1.24200E+03   1.24600E+03   1.24800E+03   1.25400E+03
   1.25800E+03   1.26000E+03   1.26400E+03   1.26600E+03
   1.26800E+03   1.26900E+03   1.27000E+03   1.27100E+03
   1.27200E+03   1.27400E+03   1.27500E+03   1.27500E+03
   1.27600E+03   1.27700E+03   1.27900E+03   1.27900E+03
   1.27900E+03   1.27900E+03   1.27900E+03   1.27800E+03
   1.27700E+03   1.27300E+03   1.27100E+03   1.27000E+03
   1.26900E+03   1.26800E+03   1.26600E+03   1.26400E+03
   1.26200E+03 )
)
```

Figure 31

Temperature profile file used to define the temperature along the boundary of the furnace wall.

The data from this trial (which was performed with the oven set to 980 ^{o}C) was then shifted uniformly upward by 20 ^{o}C because the majority of the experiments were performed with the oven set to 1000 ^{o}C. The temperature at both of the gas inlets (upstream boundaries) was set to 1240 K (967 ^{o}C) while the temperature at the gas outlet (corresponding to any backflow) was set at 1260 K (987 ^{o}C), again according to the experimental data.

Both convective and radiative heat transfer equations were used to determine the temperature in the simulation. Fluent provides several different methods for modeling radiative heat transfer, however, only the discrete ordinates (DO) model allows for the modeling of semi-transparent walls such as quartz (Fluent, Inc.). The specific details of the discrete ordinates model are beyond the scope of this work, but can be found in the Fluent documentation (Fluent, Inc.). The default settings for the angular discretization were used, and the radiation was modeled as entirely gray radiation (meaning that the emissivities involved were constant with respect to the wavelength of the radiation). In order to expedite the convergence of the solution to the flow equations, 10 flow iterations were used per radiation iteration. Additionally, both fluids (inside and outside of the nozzle) were allowed to participate in radiation.

8.3. Without Nozzle

In order to make comparisons with the control CVD setup (without a nozzle) where nanotubes are grown on substrates oriented with the active face tangent to the flow (rather than normal to the flow) a Fluent simulation was run modeling this scenario. A simple geometry was defined for a 16 cm length of furnace tube at the center of the furnace with a 1 cm chip tangent to the flow at the center of the furnace tube.

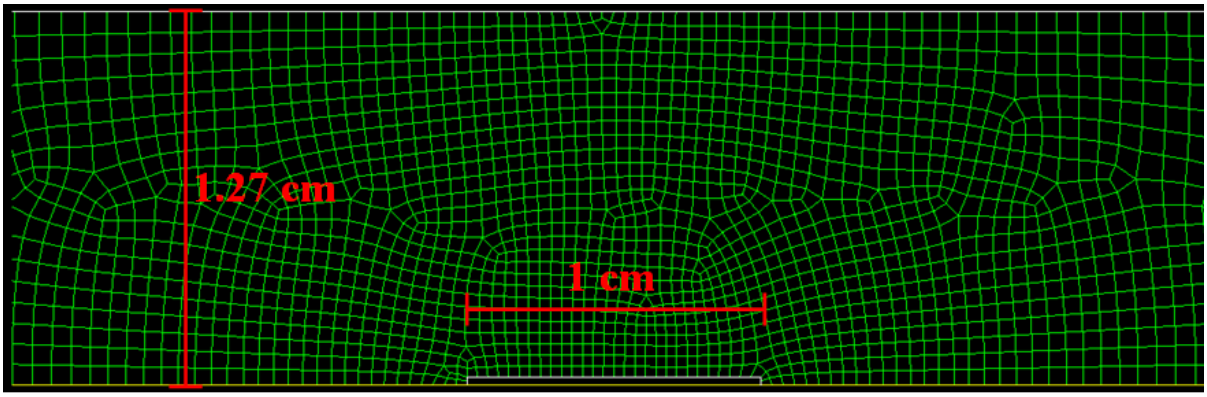

Figure 34
Central region of the grid defined for the control simulation.

A laminar flow model was then used to simulate 1 SLM of methane flowing through the entire 1 inch diameter furnace tube (argon was not included in this simulation for simplicity).

The basic results are presented in Figure 35, showing methane flow velocities of around 0.29 m/s in the center of the tube which decrease by about a factor of 2 in the area immediately surrounding the active chip face. Similarly, the associated methane pressure at the substrate was found to be extremely constant at about 0.008 pascals above the reference pressure for this particular flow rate.

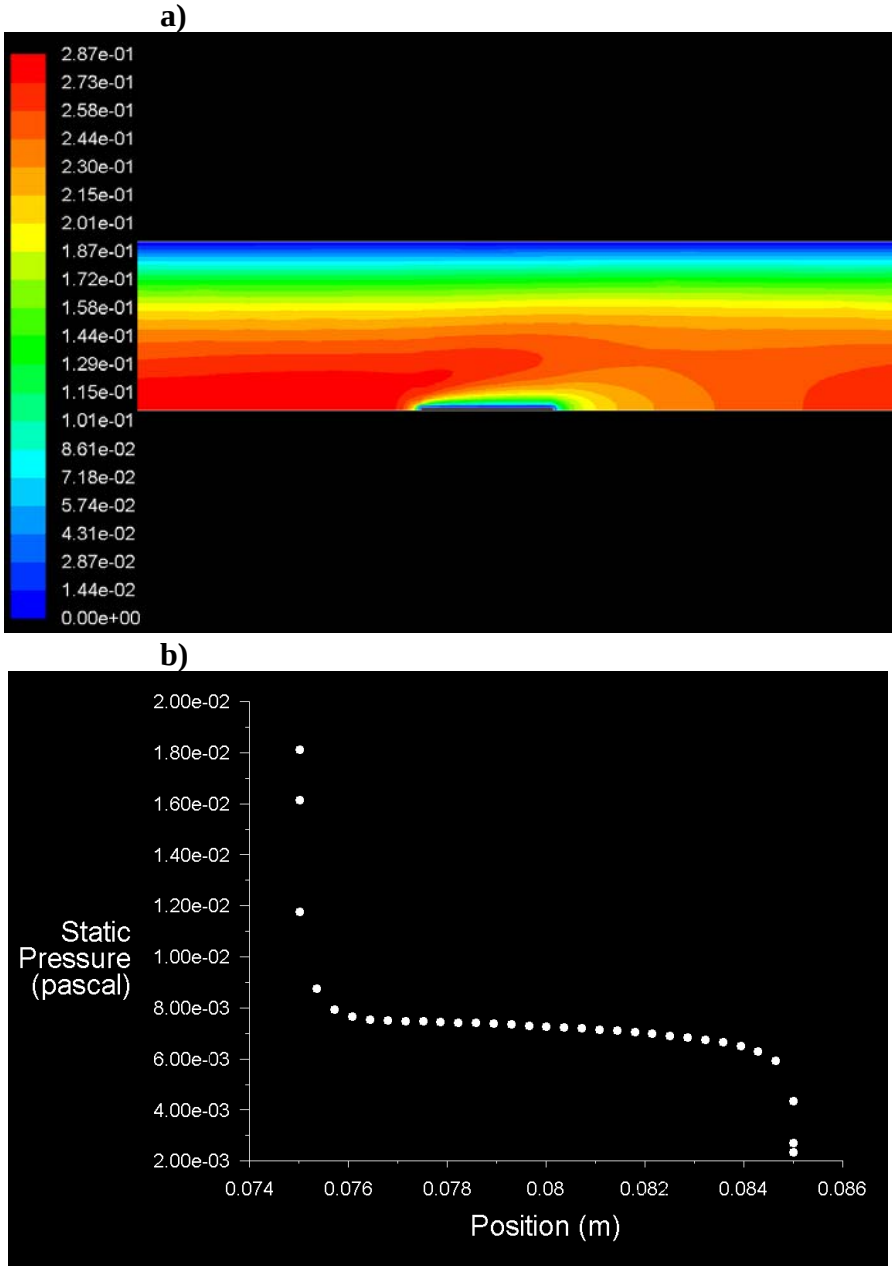

Figure 35

a) *Velocity magnitude contours and* ***b)*** *static pressure plot vs. axial position along substrate.*

8.4. Without Chip

To gain a qualitative understanding of the flow from the nozzle we ran a simulation using the nozzle, but without the silicon chip present (using only the laminar

flow model). Two different flow rates were tested for the methane inlet (inner methane flow), 100 SCCM (1.2 E-6 kg/s) and 10 SCCM (1.2 E-7 kg/s), while the flow rate around the outside of the nozzle was set to 0 for simplicity (no simulated argon flow). The results of the simulation show a substantial difference in the "spreading" of the gas stream between the high and low flow cases (Figure 36).

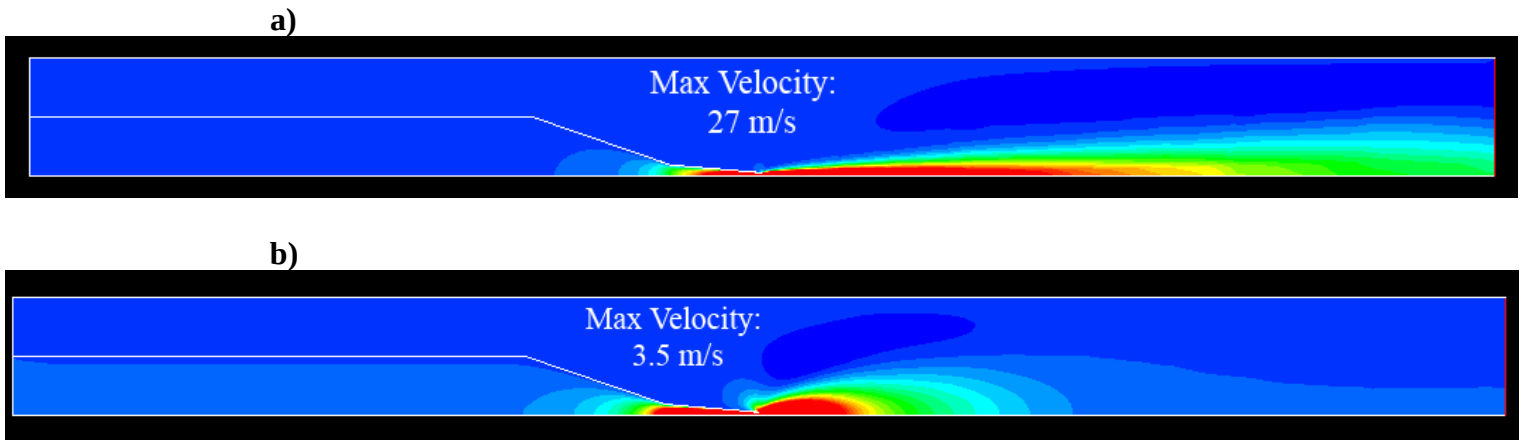

Figure 36
Axial velocity contours for the **a)** *100 SCCM methane flow case and* **b)** *for the 10 SCCM flow case.*

This is simply reflective of the differing degrees to which convective and diffusive momentum transfer occur in each case (Section 4), however it suggests that any velocity-dependant effects should be more locally confined to the center of the substrate in higher flow cases.

8.5. Flow Profiles With Substrate

Next, the simulation was repeated for the same 100 SCCM and 10 SCCM methane flow rates, this time with the substrate present. In this case we did consider the "argon" flow around the outside of the nozzle as well as the methane flow through the nozzle itself, however as previously mentioned we were unable to use the material

properties for argon as the 'outer fluid,' instead using methane for both fluids. First we discuss the case of simulating the flow profiles (rather than the temperature profiles) around the substrate for which we used an outer methane flow rate of 1.5 E-5 kg/s, simulating the mass flow rate of 0.5 SLM of argon. In this case the velocity magnitudes at the nozzle tip were 27 m/s and ~3.4 m/s for the 100 and 10 SCCM flow cases respectively (as in the similar case without the substrate). The axial velocity contours for both cases (Figures 37a and 37c) clearly show recirculation regions developing above the nozzle. These regions are even more clearly defined in the radial velocity contours which show maximum radial velocities of 12 m/s and 0.5 m/s respectively. In both cases the flows appear to be qualitatively similar.

a)

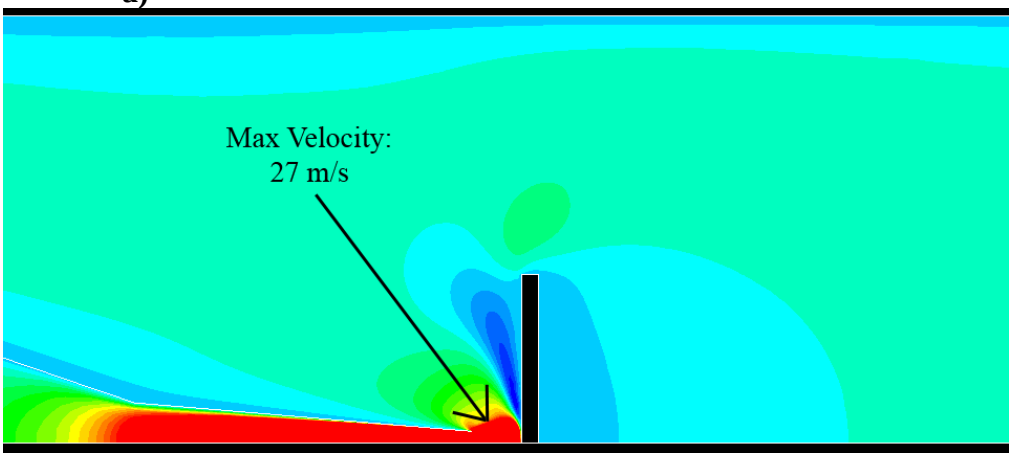

b)

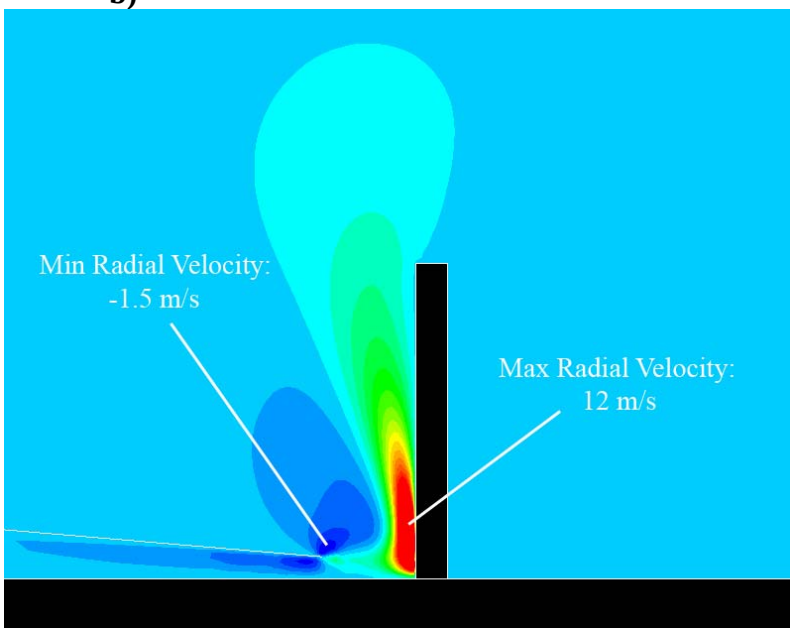
Min Radial Velocity:
-1.5 m/s
Max Radial Velocity:
12 m/s

c)

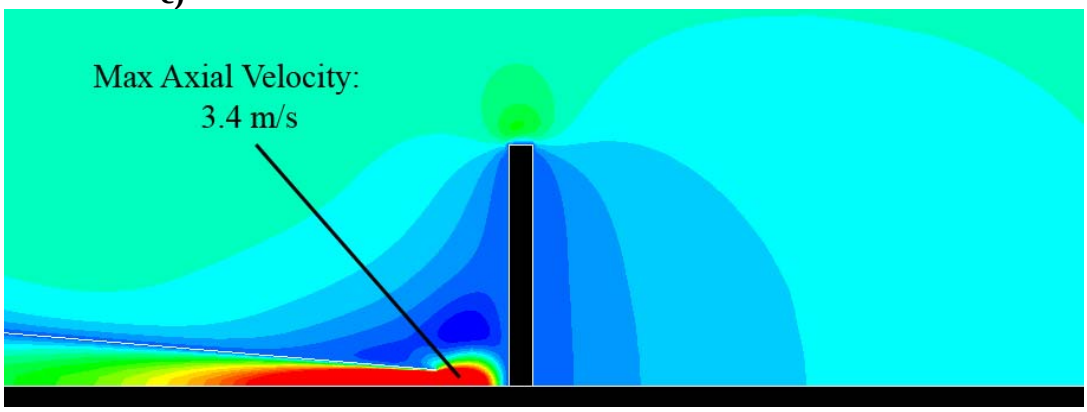
Max Axial Velocity:
3.4 m/s

d)

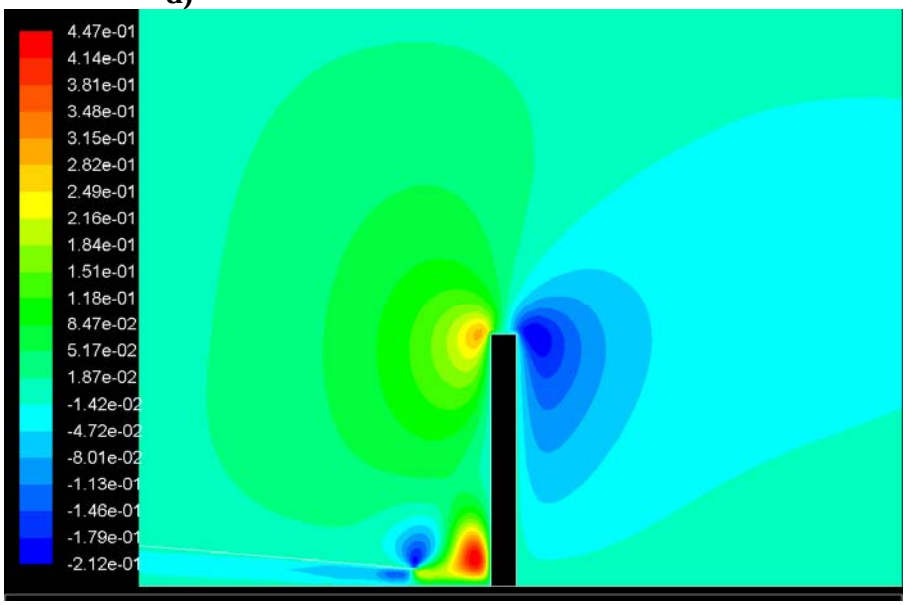

Figure 37
a) *Axial velocity contours for the 100 SCCM case* **b)** *Radial velocity contours for the 100 SCCM case* **c)** *Axial velocity contours for the 10 SCCM case* **d)** *Radial velocity contours for the 10 SCCM case.*

The primary difference between the 100 and 10 SCCM flow cases can be seen in the pressure plots given in figure 38, created by running the same simulation without any 'argon' flow (to isolate the local methane pressure at the substrate). These plots show a difference in the static pressure at the substrate in the two cases of more than a factor of 100 (with a maximum of ~50 pascals in the 100 SCCM case vs. about 0.2 pascals with 10 SCCM). It is also worth noting that there is a correspondingly steep pressure gradient in the 100 SCCM case of roughly 700 pascals/cm.

a)

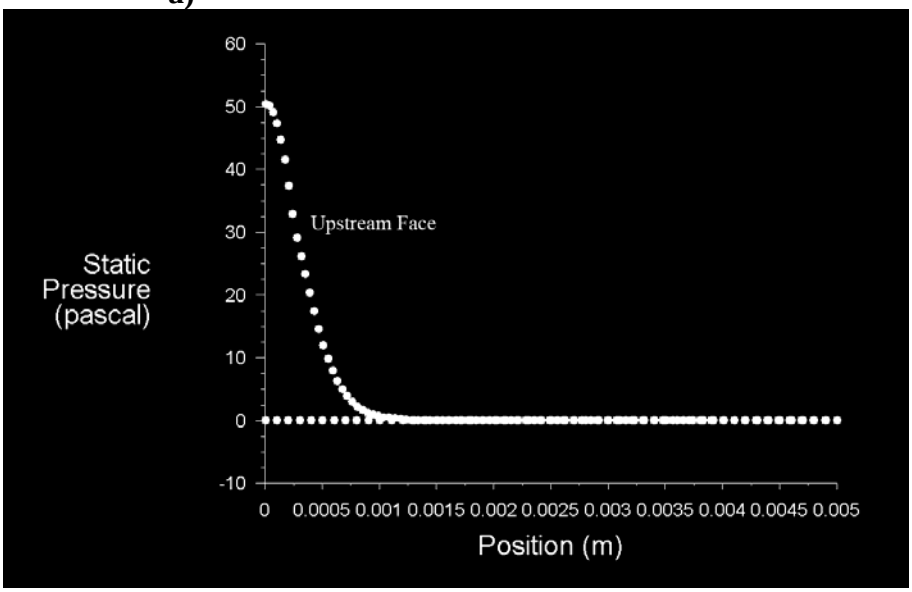

b)

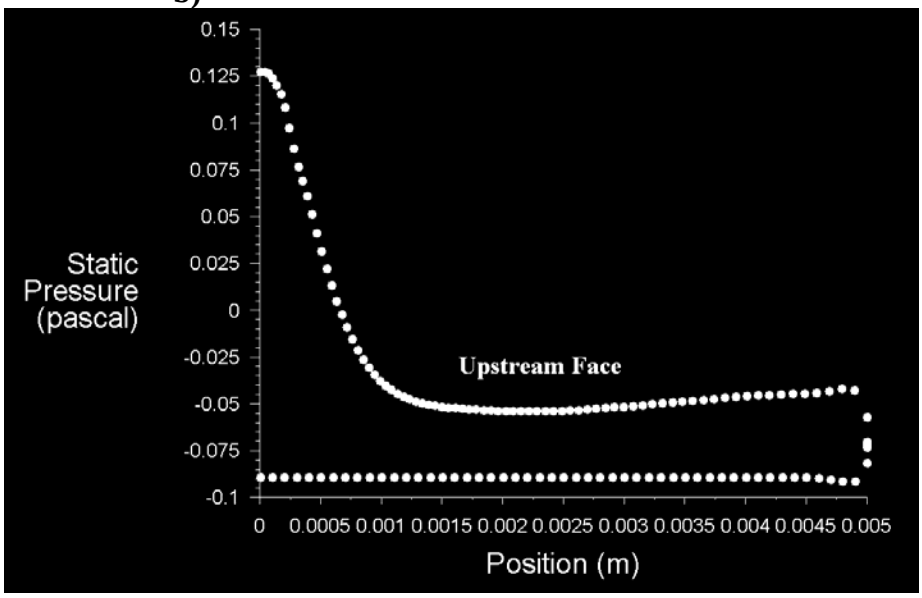

Figure 38
Static pressure (pascals) vs. radial position (m) for the upstream and downstream cases for **a)** *100 SCCM flow case* **b)** *10 SCCM flow case.*

8.6. Temperature Profiles (With Substrate)

In order to get a better understanding of the effects of methane flow rate on the temperature profile at the substrate surface, the previous simulations were run using

methane flow rates in the outer region set to approximate the heat flux of the desired argon flow rate. This meant simply adjusting the outer methane flow rate to account for the difference in heat capacity between argon and methane, giving a methane flow rate of 3.5 E-6 kg/s as the heat flux equivalent of 0.5 SLM of argon.

The first such simulation, using 100 SCCM as the inner methane flow rate, gave the temperature contours presented in figure 39.

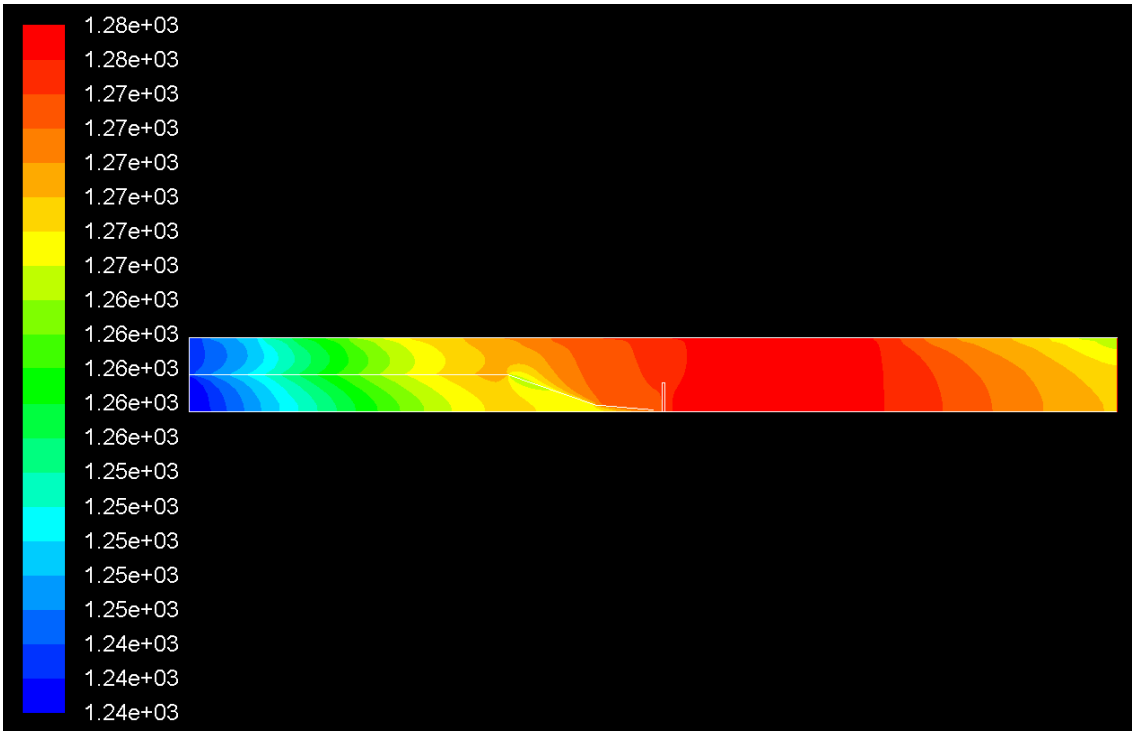

Figure 39
Temperature contours for the entire furnace tube model (temperatures given in K).

In addition to the general behavior predicted by the experimentally determined axial temperature profile, we can see the heating of the quartz tube creating a boundary layer of heightened gas temperature as expected. Looking at figures 40a and 40b we can compare the qualitative characteristics of the temperature contours surrounding the substrate predicted by the 100 SCCM and 10 SCCM methane flow simulations, and while the

differences occur entirely within a range of about 1 K, the higher methane flow rate does appear to cool the chip slightly.

a)

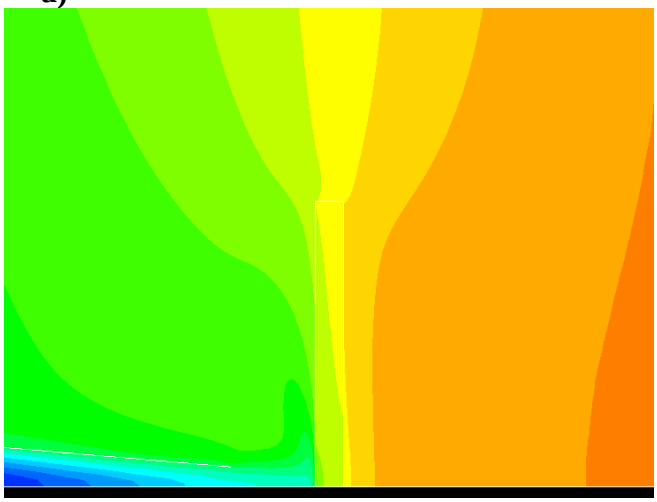

b)

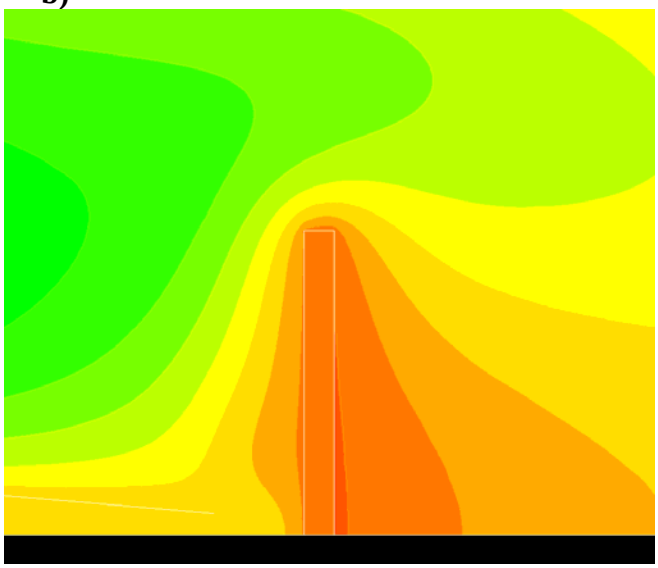

Figure 40
Closeup of the temperature contours around the substrate for the **a)** *100 SCCM flow case* **b)** *10 SCCM flow case.*

This difference can be seen more concretely by comparing the corresponding temperature profile plots (Figure 41). These plots show that in the 100 SCCM case, the temperature at the substrate increases from 1274.3 K at the center of the substrate to

about 1275.3 K at its edge. This is to be compared with a corresponding mean temperature of about 1275.0 K in the 10 SCCM case, with a temperature fluctuation of about 0.1 K over the surface of the substrate. We believe that the differences in these temperature profiles are negligeable, and that the associated temperature gradients would certainly be insignificant on the size scale of interest for nanotube growth.

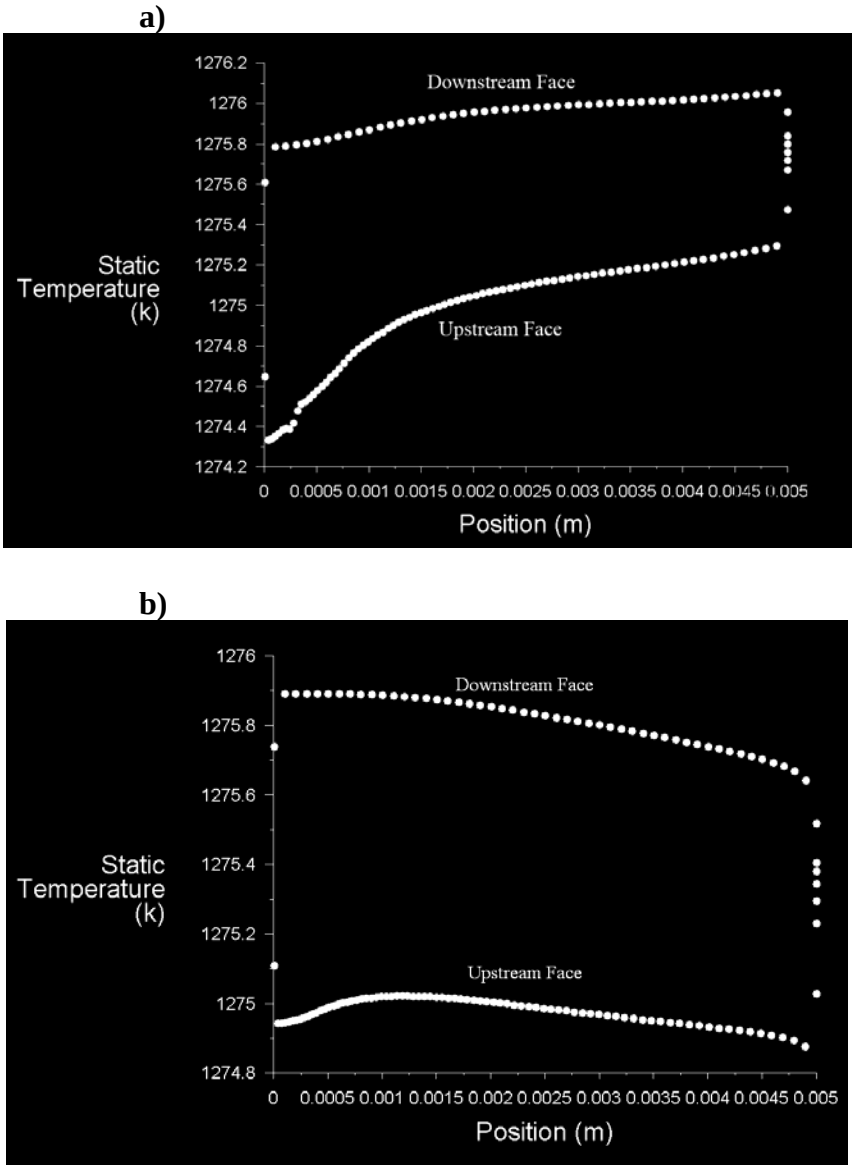

Figure 41
*Static temperature of the substrate (K) vs. radial position from the center (m) for both the upstream and the downstream faces in the **a)** 100 SCCM flow case **b)** 10 SCCM flow case.*

8.7. 2.4 mm Nozzle

In order to perform a similar simulation for the 2.4 mm nozzle experiments, the geometry and mesh were redefined with the correct nozzle aperture and nozzle-substrate distance as indicated in figure 42.

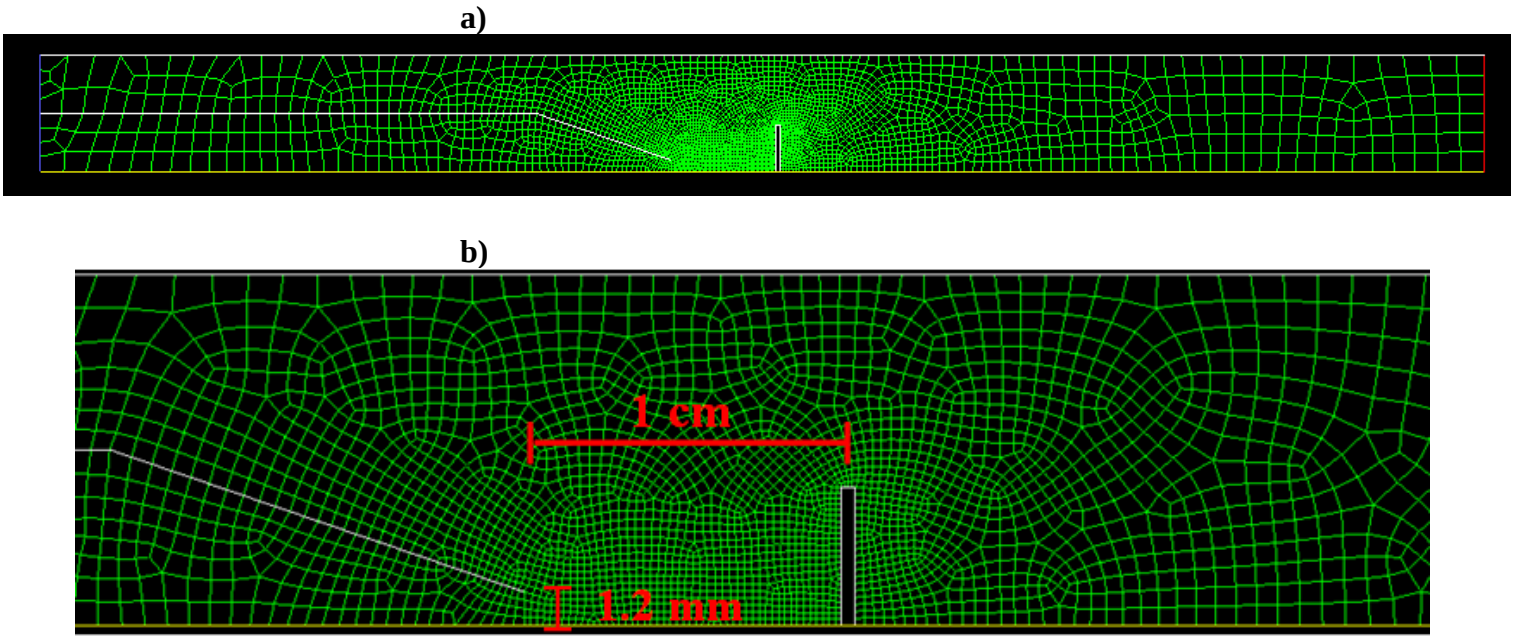

Figure 42
Meshed geometry for the 2.4 mm nozzle simulation. **a)** *Full geometry* **b)** *Closeup of center of geometry indicating relevant dimensions*

For comparison with the 0.7 mm nozzle simulations, 100 SCCM and 10 SCCM methane flow rates were used, with the rest of the simulation parameters identical to the 0.7 mm simulations. Plots of the axial velocity contours for both flow cases are given in figure 43.

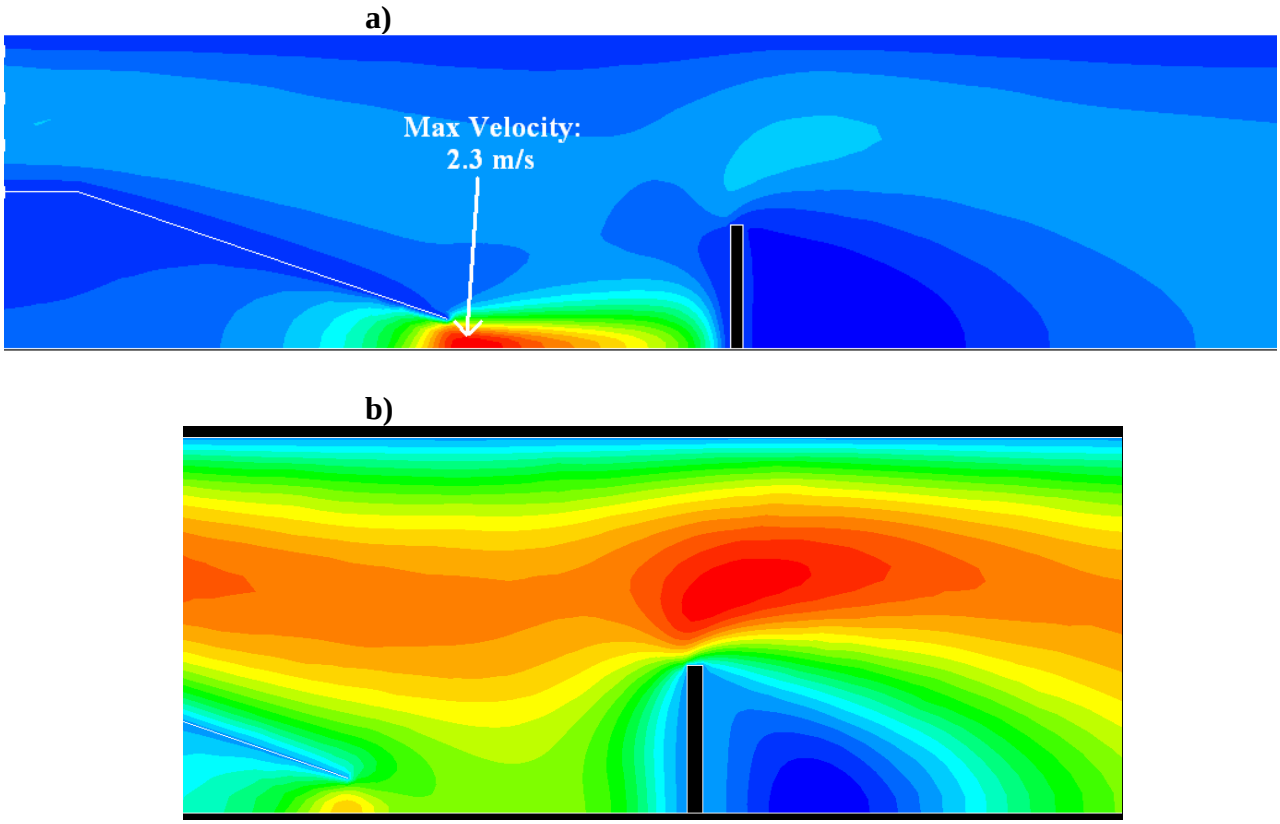

Figure 43
Axial velocity contours for **a)** *100 SCCM methane flow rate, and* **b)** *10 SCCM methane flow rate*

Two important observations can be made from figure 43. One is that the axial velocity magnitude declines very sharply between the nozzle (at 2.3 m/s) and the substrate in the 100 SCCM case. The other is that, in the 10 SCCM case, the methane flow seems to be overwhelmed by the peripheral argon flow (at least in terms of the flow velocity). If the 10 SCCM case is repeated without argon flow, we see that the methane velocity magnitude decreases from about 0.2 m/s at the nozzle to < 0.01 m/s at the substrate.

One final comparison that is useful to make is to look at the plots of static pressure along the substrate face for the 2.4 mm nozzle as compared with the 0.7 mm nozzle (Figure 44).

a)

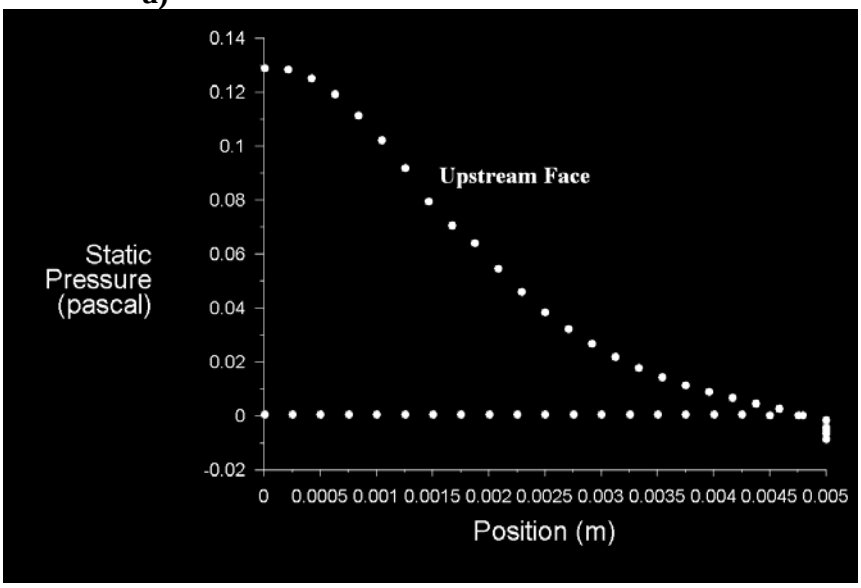

b)

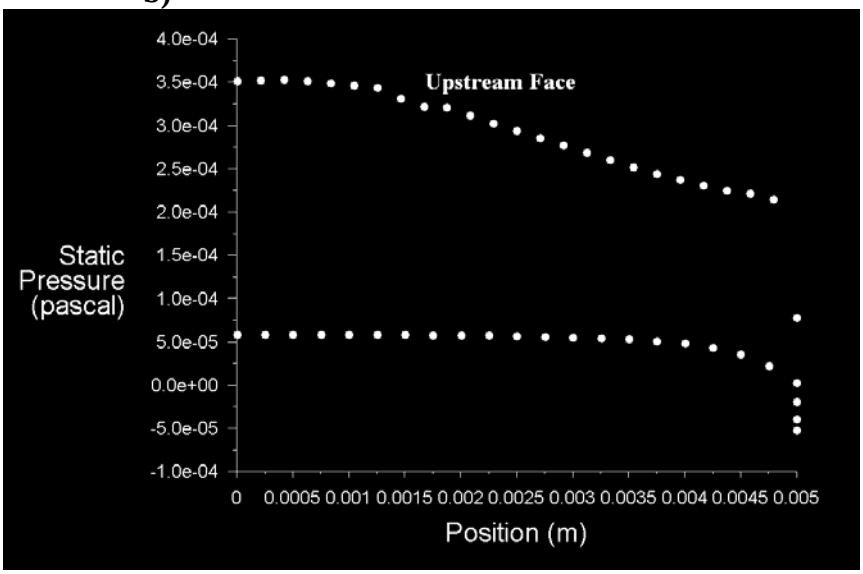

Figure 44

*Static pressure (pascals) vs. radial position along the substrate face (m) for the **a)** 100 SCCM methane flow case and **b)** 10 SCCM methane flow case*

For the 2.4 mm nozzle, the static pressure in the 100 SCCM case is roughly comparable to that in the 10 SCCM case with the 0.7 mm nozzle (still several orders of magnitude smaller than the 100 SCCM flow with the 0.7 mm nozzle). The pressure in the 10 SCCM

flow case with the 2.4 mm nozzle is reduced by yet another order of magnitude relative to this.

9. Data Analysis

9.1. Carbon Decomposition

Judging from the extensive splotch patterning observed on many of the samples we believe that carbon deposition is occurring for samples grown with the nozzle (especially with higher flow rates). This belief is supported by the fact that amorphous carbon is deposited on the quartz nozzle itself during many of the higher flow (> 50 SCCM) experiments. Because these carbon deposits tend to occur more dramatically in the higher flow cases we expect that the deposition is related to excessive methane concentration (and thus strongly correlated with methane flow rate), however we were unable to quantify the precise nature of this relationship.

Additionally, we observe a general reduction in the amount of visible alumina and we hypothesize that this could be due to an obscuring effect of the amorphous carbon deposition. Alumina densities appeared to be significantly lower than typical control values for all of the nozzle growth samples, although once again a quantitative relationship between flow rate and alumina density was not achieved. Interestingly, even at the lowest flow rate (5 SCCM) with the 0.7 mm nozzle, we found that the amount of visible alumina clusters was substantially reduced from its value in control samples. Thus, if our original hypothesis that the reduction in visible alumina is caused by an amorphous carbon layer is to be taken seriously, we must accept that heightened carbon deposition is occurring even in these extremely low flow cases.

Interestingly, we found that when we flowed 20 SCCM methane through the 2.4 mm nozzle (at a nozzle-substrate distance of ~ 1 cm) there were still strong indications of excessive carbon deposition. This is especially surprising because our Fluent model indicates that these parameters will give extremely low methane concentrations at the nozzle (Figure 45c).

a)

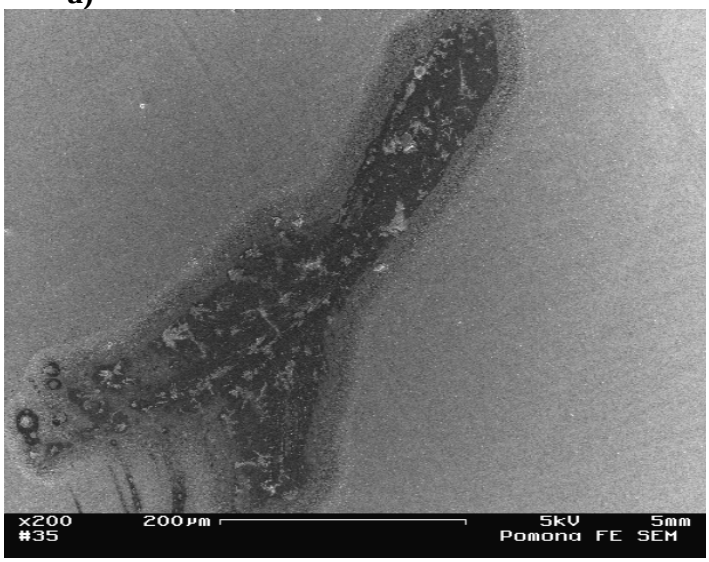

b)

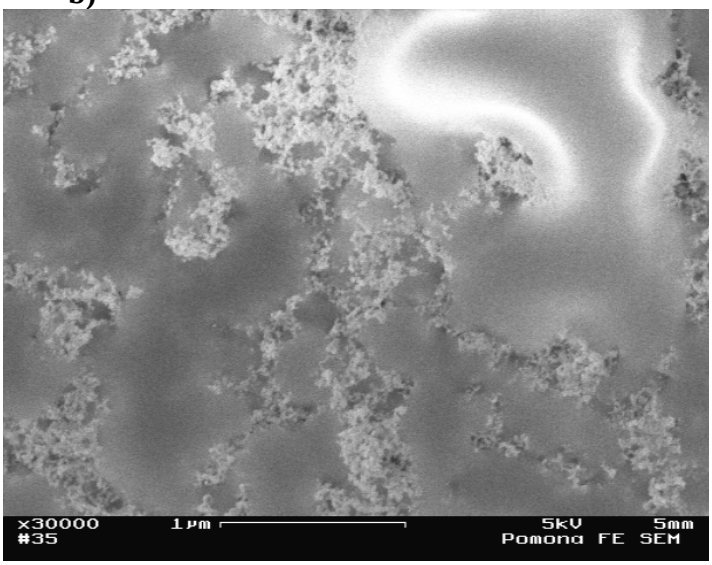

c)

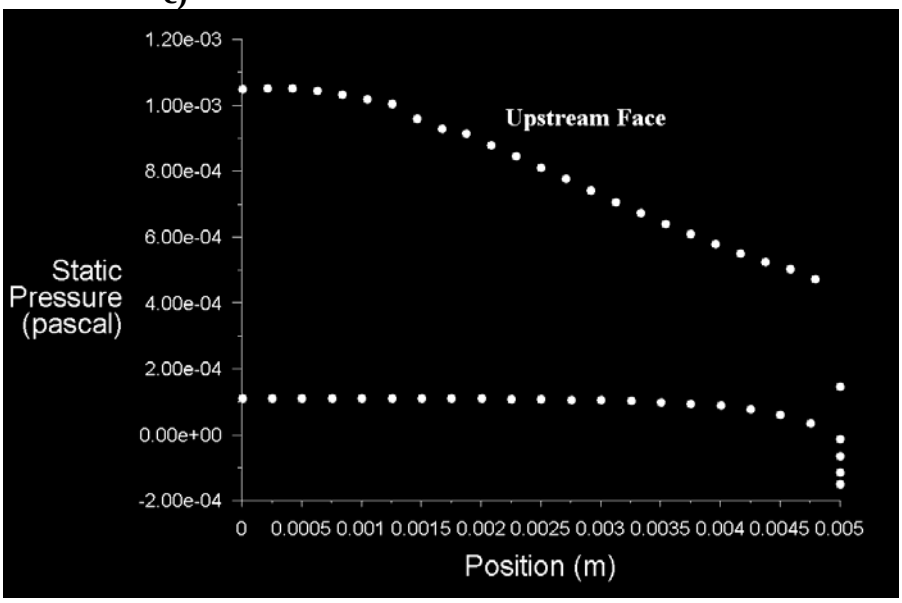

Figure 45

Data for sample grown with 2.4 mm nozzle at 20 SCCM methane flow rate. ***a)*** *SEM image indicating carbon deposition* ***b)*** *SEM image closeup of alumina cluster showing carbon layer* ***c)*** *Plot of log of the static pressure vs. radial position along the substrate.*

While clearly our hypothesis that the alumina clusters are being obscured by carbon deposits is problematic given the lack of significant available carbon in these low flow conditions, figures 45a and 45b seem to be in support of this hypothesis, showing what appear to be amorphous carbon deposits. Perhaps carbon deposition is being strongly affected by some parameter related to the nozzle flow geometry other than local methane concentration, however we are unable to provide a more satisfactory explanation at this time.

In a related finding, we observed that when samples that had previously undergone nozzle growths were put back in the furnace under control conditions they failed to grow tubes. This was verified for samples that had been run with the nozzle in both high flow (98 SCCM) and low flow (5 SCCM) cases. In the 5 SCCM case, imaging of visible alumina clusters not only showed a lack of nanotube growth, but also exhibited

what appeared to be a carbon coating surrounding (and likely covering) some of the alumina clusters (figure 46).

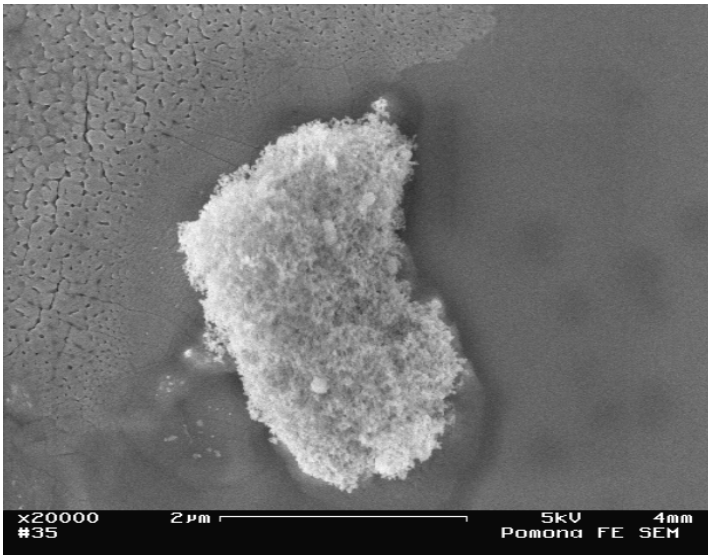

Figure 46
SEM image of alumina cluster without nanotube growth, and appearing to be coated with carbon.

Additionally, when we imaged alumina clusters near the edge of the same sample that did not have this hazed appearance, we *were* able to find some nanotubes (Figure 47).

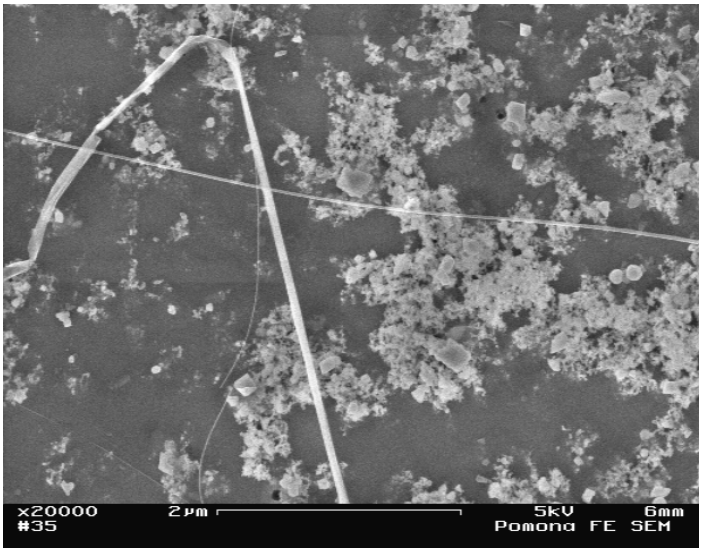

Figure 47
SEM image of low-density nanotube growth occurring in unpoisoned catalyst upon "regrowth."

These findings not only suggest that catalyst particles embedded in carbon coated alumina clusters were being inactivated ("poisoned") by the carbon deposition, but also that the severity of the poisoning decreased toward the edge of the chip (in general agreement with a methane pressure dependant model of carbon deposition). Instances of catalyst poisoning by excessive carbon deposition have been found using a variety of nanotube growth procedures including laser ablation (Scott et al., 2001), a premixed flame environment (Vander Sande et al., 2006), as well as CVD (Bonard et al., 2003). It is thus generally believed that excessive surface deposition of carbon on catalyst particles can overwhelm internal diffusion processes, decreasing the catalyst's active surface area and preventing nanotube formation, which is likely what we are directly observing in these experiments.

Given our findings it is tempting to suggest that the relevant parameter to carbon deposition is the local methane concentration (or equivalently, the partial pressure of methane along the surface of the substrate) and to compare the corresponding Fluent data for the various scenarios. For instance, the plot of static pressure along the chip surface for the control condition using a methane flow rate of 1 SLM (Figure 33b) predicts a roughly constant static pressure of 0.008 pascals relative to the operating pressure (defined at the pressure outlet). Comparing this to the results for the case of a 100 SCCM flow through the 0.7 mm nozzle we see that the methane pressure at the chip drops from 50 pascals at the center of the chip to near operating pressure at its edges. Putting pressure on a logarithmic scale (Figure 48) we see that the pressure near the chip edge is actually about 0.02 pascals (the same order of magnitude as in the control condition).

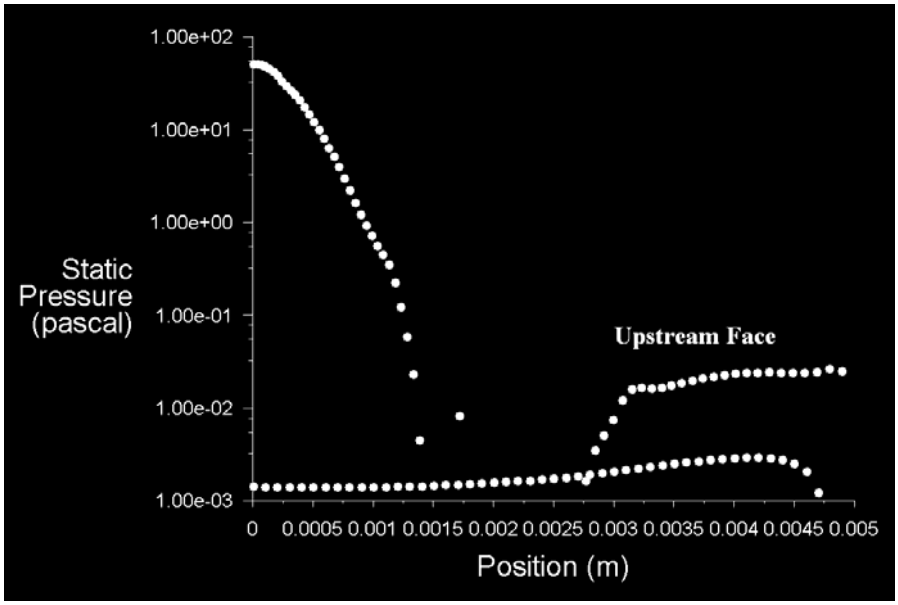

Figure 48
Plot of log of the static pressure vs. radial position along the substrate.

Similar comparisons can be made for various methane flow rates for both the 0.7 mm and 2.4 mm nozzle scenarios, and it is clear that for many of flow rates used, the indicated 'target range' of methane pressure (~ 0.01 pascals above operating pressure) should be achieved at some radius on the substrate. It is possible either 1) that these localized regions do support local nanotube growth, but that these growth regions are small and not easily detectable when imaging, 2) that the steep pressure gradient associated with the nozzle flow geometry itself is enough to cause catalyst poisoning or otherwise inactivate the growth process, or 3) that there is some parameter other than methane concentration which is contributing to carbon deposition. It is worth noting at this point that the "particle-particle interaction model" for nanotube growth (proposed for nanotubes grown in a flame environment) specifically predicts that spatially and temporally constant conditions are needed for the growth process to remain stable (Vander Sande et al.,

2005), however the extremely spatially constant pressure suggested by figure 45 for the low flow, 2.4 mm nozzle experiment likely rules out the second possibility. Considering that we only found one limited case of significant nanotube growth in all our nozzle experiments we believe the third explanation to be the most likely.

It is indeed surprising that we would be seeing these catalyst poisoning effects even at the low methane densities of our low flow rate, 2.4 mm nozzle experiments (as indicated by the Fluent simulations), especially considering that there have been numerous demonstrations of ultra high density, high yield nanotube growth both vertically and in plane (as discussed in Section 3.3.3) which clearly do not suffer catalyst poisoning even with substantial methane concentrations. A more appropriate analysis would take into account not only the reaction kinetics of the 'cracking' decomposition reaction, but also the details of the three reaction processes (decomposition, diffusion and precipitation) involved in nanotube growth (Section 3.4), in order to consider any potentially relevant parameters (such as chemical contamination on the nozzle or substrate) beyond methane concentration. Unfortunately, such an analysis is beyond the scope of this work. It is interesting to note that researchers have experimentally demonstrated (Hata et al., 2004) that the carefully controlled introduction of water vapor into the furnace during CVD growth provides a weak oxidizer that can remove amorphous carbon and thus preserve catalyst activity. This leads us to believe that the detailed chemical environment at the substrate could be more significant than we have accounted for.

Furthermore, we can compare these possibilities with our previous findings when flowing the methane through the optical fiber with these possible explanations. The fact

that these experiments showed similar indications of carbon deposition and catalyst poisoning, even though we estimated flow rates to be ~ 0.1 SCCM (with corresponding methane velocities at the fiber tip roughly equal to velocities in control conditions) provides further support for the possibility that there is some unaccounted for parameter that is contributing to carbon deposition.

9.2. Observed Nanotube Growth

Considering that we only really have one instance of substantial (local) nanotube growth, we are unable to make any real conclusions about the necessary parameters. It was initially tempting to suggest that because the flow rate used was 680 SCCM, and because the observed region of nanotube growth was near the edge of the chip where methane pressures were the lowest that there would be some flow rate < 680 SCCM that would yield larger regions of successful tube growth. After thoroughly exploring this region of parameter space without success, we demonstrated the lack of nanotube growth when continuously varying the flow rate from 5 SCCM to 150 SCCM. Because our simulation indicates that the methane pressures found in control experiments should be encountered within this range, we take this result as an indication that the carbon deposition process is not solely dependant on methane pressure.

9.3. Evaporated Catalysts Samples

The results of our experiments with evaporated catalyst served to further complicate this analysis. Firstly, substantial multi-walled nanotube growth was observed on top of what we believe were regions of amorphous carbon deposition, only for a flow rate of 30 SCCM, and only in one instance (with a particular iron evaporation thickness). No single-walled carbon nanotubes were found in these regions, and no tubes of any kind

were found in or around the catalyst pads for any of the flow rates or iron film thicknesses tested. Because multi-walled nanotubes are believed to form when carbon diffusion, rather than deposition, is the rate limiting process (Hafner et al., 1998), the observed formation of large, multi-walled tubes agrees with the general notion that the nozzle flow is leading to excessive catalytic carbon decomposition. It would certainly be interesting to experiment with higher flow rates to see if the formation of MWNTs would increase accordingly.

We believe that we were unable to show any nanotube growth with the evaporated catalyst when using the nozzle because of the same catalyst poisoning effects apparent with solution-based catalyst samples. The fact that we observe carbon deposition (this time in the form of large blobs covering the catalyst pads) for the higher flow case and not in the lower flow cases agrees with our findings for the solution based catalyst samples. Interestingly, however, there were no significant indications of catalyst "obscuring" effects in any of the evaporated catalyst samples while these effects seemed quite noticeable for the corresponding flow rates with the solution based catalyst. It thus seems that either this effect is particular to the alumina supported iron, or that our interpretation of those results was incorrect.

9.4. Speculations

If we are correct in our interpretation that our failure to achieve nanotube growth with the nozzle technique is due to excessive carbon decomposition, our analysis becomes one of largely attempting to understand why this deposition process would be enhanced by the nozzle flow. One obvious difference between the nozzle and control growths is the orientation of the substrate relative to the gas stream. As previously

described, we found that even when methane was flowed throughout the entire furnace tube, nanotubes did not grow on a vertically oriented chip if the flow rate was high enough. This finding immediately suggests that the crucial difference is one of methane pressure rather than some effect particular to the nozzle flow (such as effects of rapid gas expansion). We hypothesize that the process preventing nanotube growth in the vertically oriented control samples is the same process (catalyst poisoning through excessive carbon decomposition) occurring in the nozzle growths. This belief is supported by the finding that the vertically oriented chips showing no growth failed to show nanotube growth in subsequent runs where they were oriented tangent to the flow. The likely explanation for this is once again poisoning of the catalyst particles by carbon deposition, the amorphous carbon coatings would in this case simply be too thin to image with the electron microscope. It then follows that a similar process of catalyst poisoning without visible carbon deposition is occurring both for the low flow rate nozzle samples as well as the sample oriented tangent to the 2.4 mm nozzle. It is possible that both the vertical orientation of the substrate and the nozzle gas flow could individually be promoting the carbon decomposition process. This would explain why we observe the most obvious signs of carbon deposition when both of these factors are present.

The fact that we were even unable to grow nanotubes with the nozzle when the substrate was oriented tangent to the flow further suggests that a more sophisticated model for the failure of nanotube formation is needed. There are likely a number of uncontrolled parameters in our experiment that could be having unforeseen effects on the growth process ranging from differences in catalyst preparation and age to the cleanliness

of the nozzle and substrate. Clearly, however, more experiments will have to be run before any further claims can reasonably be made as to what these factors might be.

10. Future Directions

There is an almost overwhelming region of parameter space that could be explored to investigate the source(s) of these strange results, and many of these parameters could be studied with simple manipulations of the flow geometry. For instance, using larger nozzle apertures, different nozzle-substrate distances, or even substrate orientations (positioning the substrate at various angles relative to the flow) could help to distinguish orientation-dependant effects from any nozzle-dependant ones. Clearly, as the nozzle aperture size and the nozzle-substrate distance increase we expect that the experiment will become essentially identical to the control experiment at some point, and it would be interesting to see the parameters for which nanotube growth is first observed. Attempts at manipulating the fine structure of the flow geometry and partial pressure could even be made by performing similar experiments on substrates with lithographically defined 3-dimensional structures (such as channels of various widths).

In general our experiment suffered from the lack of quantified observations. Along these lines, the use of Raman spectroscopy in addition to SEM imaging could be used to perform faster, more quantitative assessments of nanotube growth. Similarly, precise weighing of samples before and after growths would provide data of the mass of material deposited during growth, which when combined with Raman data could allow quantification of both nanotube and amorphous carbon yields.

One simple experiment that would help to clarify issues of carbon deposition would be to vary the duration of the methane flow (as well as the flow rate) in order to

compare the various deposition rates with the observed morphologies of (what we believe to be) amorphous carbon. It would also be important, in a further investigation of these results, to explore a wider range of methane flow rates with the 2.4 mm nozzle as well as potentially obtaining a finer flow-controller to explore flows even lower than 5 SCCM. A far more extensive comparison of nozzle growths with solution based and evaporated catalyst would be interesting as well as a comparison of the effects of changing source gases from methane to ethane or ethylene.

Perhaps the most promising continuation of this work, however, would be to add controlled concentrations of water vapor to the CVD furnace during growth in order to oxidize excessive amorphous carbon deposits and prevent catalyst poisoning, as demonstrated in (Hata et al., 2004). Considering that Hata et al. were able to demonstrate these catalyst preserving effects for a variety of catalysts (including alumina supported iron) using extremely low source gas (ethylene) flow rates (10 – 150 SCCM), it seems likely that this technique could prove extremely valuable in achieving nanotube growth with the nozzle CVD method.

11. Conclusions

As a means of studying the effects of source gas flow geometry on nanotube growth, we modified the CVD apparatus to flow methane through either a 0.7 mm or a 2.4 mm nozzle. If proven effective, gas-injection nozzles could be used in the CVD growth of nanotubes to attain precise control over the location (and possibly other properties) of the nanotubes grown by allowing the targeted delivery of source gas on almost any type of substrate. In attempting to use this nozzle CVD apparatus to grow nanotubes we explored the usage of both alumina supported iron catalyst solution and

evaporated iron thin films, as well as a wide range of methane flow rates and nozzle-substrate distances. None of these experiments showed substantial nanotube growth, instead consistently yielding samples that appeared to show signs of excessive carbon deposition.

In the experiments using the solution-based catalyst, there was a significant reduction in the amount of alumina clusters visible in the SEM relative to control samples grown without the nozzle. Additionally, in some of the cases with higher methane flow rates we saw clear signs of amorphous carbon deposition in the SEM images. When using the evaporated catalyst the effects were qualitatively different, although we believe them to be the result of the same carbon deposition process. In the 'high flow rate' condition (30 SCCM) with the 2.4 mm nozzle, we observed large blobs of amorphous carbon covering many of the 'pads' of evaporated catalyst, on top of which we found MWNTs. For both catalysts, experiments with low flow rates tended not to show the same dramatic signs of carbon deposition; however, even in these cases we did not observe nanotube growth. These observations, combined with the fact that the quartz nozzle tubing itself was left coated with amorphous carbon after experiments with high methane flow rates, lead us to believe that increased methane decomposition is the primary factor preventing nanotube growth in these experiments.

Additional experiments showing that the growths using the nozzle were actually poisoning the catalyst further corroborated the carbon deposition hypothesis. In these experiments, samples that failed to show nanotube growth after CVD runs with the nozzle were but back in the CVD furnace and failed to show nanotube growth under control conditions. This was true for both high (100 SCCM) and low (5 SCCM) methane

flow cases, and was true even for regions of the sample that did not appear in SEM images to be coated by amorphous carbon layers. We believe that even in these cases the catalyst is being deactivated ('poisoned') by thin amorphous carbon layers, and that this process is occurring for both the solution-based and evaporated catalyst samples.

Interestingly, these catalyst poisoning results were also found without the nozzle when we used high (~ 4.5 SLM) methane flow rates with the substrate oriented vertically in the furnace. In this same case, a horizontally oriented chip demonstrated normal nanotube growth while the vertically oriented chip showed no tube growth and exhibited catalyst poisoning effects. Because the methane pressures at the substrate are higher for substrates oriented normal to the gas flow, these results would support the view that high methane pressures are producing the excessive carbon deposition.

In order to better understand the relevant gas flow parameters in the growths a computational fluid dynamics simulation of the experiment was created using Fluent 6.2.16. Our initial guess as to the cause of the observed amorphous carbon deposition was that the concentrations of methane at the substrate were too large. Therefore, the most important findings of the simulation were regarding methane pressures at the substrate surface for various flow conditions (for a detailed discussion of all the results of the simulation see Section 8). Firstly, our simulation shows that the methane pressure at the substrate surface in control conditions was very low (around 0.01 pascals above atmospheric pressure) and had high spatial uniformity. In contrast, with the 0.7 mm nozzle, there was an extremely sharp pressure gradient in the high flow conditions (still somewhat present in the low flow conditions), even though the pressure near the edge of the substrate was comparable to its value in the control condition. Furthermore, for

simulations with the 2.4 mm nozzle we saw that, when using low flow rates, the methane pressure at the substrate was very uniform and more than an order of magnitude lower than control values. This was very surprising considering that the corresponding experimental condition (20 SCCM through the 2.4 mm nozzle at a substrate-nozzle distance of 1 cm) showed clear indications of excessive carbon deposition. This important result seems to suggest that attributing the carbon deposition to increased methane concentration at the substrate is probably inaccurate.

It is extremely difficult to draw any solid conclusions from this work, except that given our specific growth parameters the nozzle apparatus doesn't support nanotube growth. Additionally, it seems highly likely that the reason the nozzle experiments were not yielding nanotubes is due to poisoning of the catalyst particles by amorphous carbon deposition. Beyond this, we are unable to construct a hypothesis to explain these results that is consistent both with our experimental findings and with the results of our fluid dynamics simulation. It will thus be necessary to pursue further experimentation along these lines in order to better understand these effects.

12. Bibliography

Avouris P. Molecular electronics with carbon nanotubes. *Acc. Chem. Res.* **2002**, 35, 1026-1034.

Awasthi K, Srivastava A, Srivastava ON. Synthesis of carbon nanotubes. *Journal of Nanoscience and Nanotechnology* **5** (10): (2005) 1616-1636.

Balbuena PB, Martinez-Limia A, Zhao J. Understanding catalysed growth of single-walled carbon nanotubes. *Nanotechnology* **16** (2005) S575-S581.

Baughman RH, Zakhidov A, de Heer W. Carbon nanotubes – the route toward applications. *Science* **297** (2002) 787-792.

Bonard JM, Croci M, Klinke C, Conus F, Arfaoui I, Stockli T, Chatelain A. Growth of carbon nanotubes characterized by field emission measurements during chemical vapor deposition. *Phys. Rev. B* **67** (2003)

Choi YC, Shin YM, Lee YH, Lee BS, Park GS, Choi HM, Lee NS, Kim JM. Controlling the diameter, growth rate, and density of vertically aligned carbon nanotubes synthesized by microwave plasma-enhanced chemical vapor deposition. *Applied physics letters* **17** (2000) 2367.

Dai H.; Rinzler A.G.; Nikolaev P.; Thess A.; Colbert D.T.; Smalley R.E. Single-wall nanotubes produced by metal-catalyzed disproportionation of carbon monoxide. *Chem. Phys. Letters* **260**, No. 3 (1996) 471-475.

De Heer WA, Wang Z, Poncharal P, Frank S. Carbon Nanotube Quantum Resistors. *Science* **280** (1998) 1744 – 1746.

Derbyshire F, Dickey E, Mao Z, Rao A, Qian D, Andrews R, Sinnot S. Model of carbon nanotube growth through chemical vapor deposition. *Chem. Phys. Letters* **315** (1999) 25-30

Dupuis, Anne-Claire. The catalyst in the CCVD of carbon nanotubes—a review. Progress in Materials Science, **50**, (2005) 929-961.

Iijima S. Helical microtubules of graphitic carbon. *Nature* **354**, 56 (1991)

Ferguson, Matthew. Steps toward the creation of a carbon nanotube single electron transistor. Senior Thesis, Pomona College Physics (2003).

Fluent 6.2 Documentation. <C:\Fluent.Inc\fluent6.2.16\help\index.htm>. Fluent, Inc.

Frank, I. Tanenbaum, D. Unpublished research. Personal Correspondence. 2005.

Gambit 2.2 Documentation. <C:\Fluent.Inc\gambit2.2.30\help\index.htm>. Fluent, Inc.

Guyon E, Hulin J-P, Petit L, Mitescu C. Physical Hydrodynamics. Oxford University Press: New York, 2001.

Haddon R, Itkis M, Sen R, Bhowmik P, Zhao B, Hu H, Hamon M, Niyogi S. Chemistry of single-walled carbon nanotubes. *Acc. Chem. Res.* **35** (2002) 1105-1113.

Hafner J, Bronikowski M, Azamian B, Nikolaev P, Rinzler A, Colbert D, Smith K, Smalley R. Catalytic growth of single-wall carbon nanotubes from metal particles. *Chemical Physics Letters* **296** (1-2) (1998) 195-202.

Hata K, Futaba D, Mizuno K, Namia T, Yumura M, Iijima S. Water-assisted highly efficient synthesis of impurity-free single-walled carbon nanotubes. *Science* **306** (2004) 1362.

Hilding, J.M.; Hong, M.P.L. ; Grullke, E.A. Alignment of dispersed multiwalled carbon nanotubes in low strength AC electrical fields. *Journal of Nanoscience and Nanotechnology* 5, no. 5, (May 2005) : 742-6

Hirsch, Andreas. Functionalization of single-walled carbon nanotubes. *Angew. Chem. Int. Ed.* **41** (2002), No. 11.

Hone J, O'Brien S, Sfier M, Huang M, Jun S, Huang L, Caldwell R, Huang X. Controlled placement of individual carbon nanotubes. *Nanoletters* **5** No. 7 (2005) 1515-1518

Huang, S. Cai, X. Liu, J. Growth of Millimeter-Long and Horizontally Aligned Single-Walled Carbon Nanotubes on Flat Substrates. *J Am. Chem. Soc.* **125(19)** (2003) 5636.

Kappes M, Lohneysen H, Hennrich F, Krupke R. Separation of metallic from semiconducting single-walled carbon nanotubes. *Science* **18** Vol. 301. no. 5631, pp. 344-347 (2003).

Kong J, Cassel A, Dai H. Chemical vapor deposition of methane for single-walled carbon nanotubes. *Chemical Physics Letters* **292** (1998) 567-574.

Li CH, Tseng SC, Lo SC, Chen KF, Juang ZY, Leou KC, Tsai CH. Pressure effect of low-temperature growth of multi-wall carbon nanotubes on Nickel catalyst/barrier-coated glass by thermal-CVD. *Surface & Coating Technology* **200** (10) (2006) 3220-3223.

Lieber C, Hafner J, Odom TW. Scanning probe microscope studies of carbon nanotubes. *Topics in Applied Physics* **80** (2001) 173-211.

Maruyama S, Okubo T, Ogura M, Hu M, Miyauchi Y, Chiashi S, Murakami Y. Growth

of vertically-aligned single-walled carbon nanotube films on quartz substrates and their optical anisotropy. *Chem Phys Letters* **385** (2004) 298-303.

McFarland J and Scire E. Unpublished research. 2002.

Nagahara L, Ribayrol A, Burgin T, Lewenstein J, Tsui R. High-yield selective placement of carbon nanotubes on pre-patterned electrodes. *Nanoletters* (2002) **2** No. 5, 443-446.

"NanoMaterials Project." <http://mmptdpublic.jsc.nasa.gov/jscnano/> Johnson Space Center. (11/30/05).

Penilla E. Senior thesis research in progress (unpublished). Personal Communication, 2006.

Provencio P, Siegal M, Bush P, Wang J, Xu J, Huang Z, Ren Z. Synthesis of Large Arrays of well-aligned carbon nanotubes on glass. *Science* **6** Vol. 282. no. 5391, pp. 1105–1107 (1998).

Qian L, Li W, Zhou W, Liu W, Li L, Wang C, Chang B, Xie S, Pan Z. Very long carbon nanotubes. *Nature* **394**, (1998) 631 - 632

Rueckes T, Kim K, Joselevich E, Tseng G, Cheung C, Lieber C. Carbon Nanotube-Based Nonvolatile Random Access Memory for Molecular Computing Science **289** (2000) no. 5476, pp. 94 – 97.

Salernitano E, Lisi N, Giorgi R, Giorgi L, Makris D. CNT growth on alumina-supported nickel catalyst by thermal CVD. *Diamond and Related Materials* **14** (2005) 815-819.

Schlapback L, Emmenegger C, Groening O, Kuttel O. Electron field emission from phase pure nanotube films grown in a methane/hydrogen plasms. *Applied Phys. Letters* (1998) **73** (15) 2113-2115.

Scott, CD, Arepalli S, Nikolaev P, Smalley RE. Growth mechanisms for single-wall carbon nanotubes in a laser-ablation process. *Applied Physics A: Materials Science & Processing* **72** 5 (2001), 573-580.

Smalley R, Smith K, Colber D, Rohmund F, Bradley K, Bronikowski M, Nikolaev P. Gas-phase catalytic growth of single-walled carbon nanotubes from carbon monoxide. *Chem Phys Letters* **313** (1999) 91-97.

Vander Sande J, Tester J, Howard J, Height M. Carbon nanotube formation and growth via particle-particle interaction. *J. Phys. Chem. B.* **2005**, *109*, 12337-12346.

Williams PA, Papadakis SJ, Falvo MR, Patel AM, Sinclair M, Seeger A, Helser A, Taylor II RM, Washburn S, Superfine R. Controlled placement of an individual carbon nanotube onto a microelectromechanical structure. *Applied Physics Letters* **80**, 14, (2002) 2574-2576.